JOURNAL OF OPTOELECTRONICS AND ADVANCED MATERIALS Vol. 10, No. 7, July 2008, p. 1535 - 1563

Review paper

Fermi surface properties and unconventional superconductivity in rare earth, uranium and transuranium compounds

Y. ŌNUKI[a,b,*], R. SETTAI[a], H. SHISHIDO[c], S. IKEDA[b], T. D. MATSUDA[b], E. YAMAMOTO[b], Y. HAGA[b], D. AOKI[d], H. HARIMA[e], H. HARIMA[e], H. YAMAGAMI[f]

[a]*Graduate School of Science, Osaka University, Toyonaka, Osaka 560-0043, Japan*
[b]*Advanced Science Research Center, Japan Atomic Energy Agency, Tokai, Ibaraki 319-1195, Japan*
[c]*Graduate School of Science, Kyoto University, Kyoto 606-8501, Japan*
[d]*Institute for Materials Research, Tohoku University, Oarai, Ibaraki 311-1313, Japan*
[e]*Department of Physics, Faculty of Science, Kobe University, Kobe 657-8501, Japan*
[f]*Department of Physics, Faculty of Science, Kyoto Sangyo University, Kyoto 603-8555, Japan*

We studied the various kinds of electronic states in the *f*-electron systems of the cubic RX_3 and AnX_3 compounds and the tetragonal RTX_5 and $AnTX_5$ compounds (R: rare earth, An: Th, U, Np, Pu, T: transition metal, X: Al, Ga, In, Si, Ge, Sn) through the de Haas-van Alphen experiment and the energy band calculation. The former compounds are three dimensional in the electronic states, while the latter compounds are quasi-two dimensional. Pressure experiments were also carried out for antiferromagnets $CeIn_3$ and $CeRhIn_5$ to change the electronic state from the antiferromagnetically ordered state to the non-magnetic state, crossing the critical pressure region where the Néel temperature becomes zero. Around this critical pressure region, *d*-wave superconductivity is induced, and a marked change of the Fermi surface properties from the 4*f*-localized state to the 4*f*-itinerant state occurs at this critical pressure, revealing the first-order phase transition.

(Received April 1, 2008; accepted June 30, 2008)

Keywords: Rare earth compounds, Actinide compounds, de Haas-van Alphen effect, Fermi surface

1. Introduction

The 4*f* (5*f*) electrons in the rare earth (actinide) atoms are pushed deep into the interior of the closed $5s^25p^6$ ($6s^26p^6$) shells because of the strong centrifugal potential $\ell(\ell+1)/r^2$, where $\ell = 3$ holds for the *f* electrons. This is the reason why the *f* electrons possess an atomic-like character even in a compound. The localized *f*-electron picture is a good starting point in magnetism, especially in the rare earth compounds. On the other hand, the tail of their wave function in the *f*-electron compounds spreads to the outside of the closed $5s^25p^6$ ($6s^26p^6$) shells because it is highly influenced by the potential energy, the relativistic effect, the distance between the rare earth (actinide) atoms, and hybridization of the *f* electrons with the conduction electrons.

The *f* electrons of cerium and uranium compounds exhibit a variety of characteristic features including spin and charge orderings, spin and valence fluctuations, heavy fermions and anisotropic superconductivity [1-3]. In these compounds, the Ruderman-Kittel-Kasuya-Yosida (RKKY) interaction and the Kondo effect compete with each other. The RKKY interaction enhances the long-range magnetic order, where the *f* electrons with magnetic moments are treated as localized electrons, and the indirect *f-f* interaction is mediated by the spin polarization of the conduction electrons. The intensity of the RKKY interaction is proportional to the square of the magnetic exchange interaction J_{CF} between the *f* electrons and conduction electrons, and the corresponding ordering temperature is characterized by

$$T_{RKKY} \propto D(\varepsilon_F)\left|J_{CF}\right|^2 \qquad (1)$$

where $D(\varepsilon_F)$ is the electronic density of states at the Fermi energy ε_F .

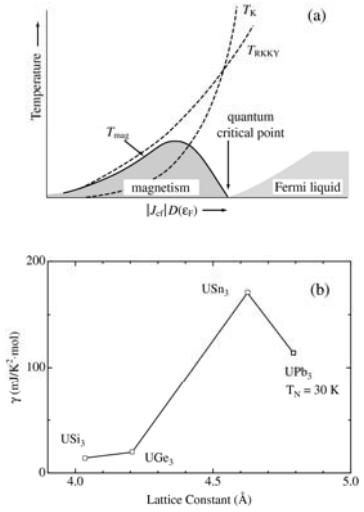

Fig. 1. (a) Doniach phase diagram and (b) the γ vs lattice constant in UX_3.

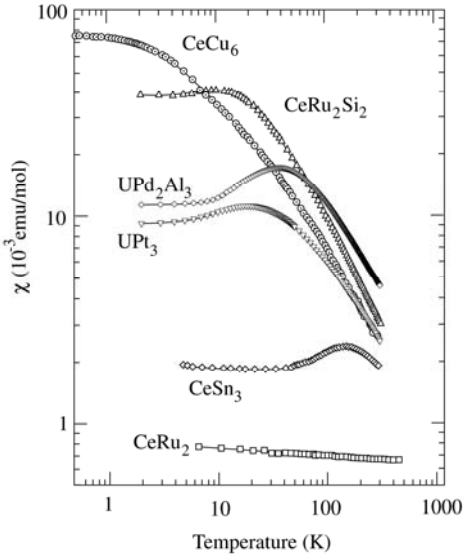

Fig. 2. Temperature dependence of the magnetic susceptibility in the typical cerium and uranium compounds.

On the other hand, the Kondo effect quenches the magnetic moments of the localized *f* electrons by the spin polarization of the conduction electrons, producing a spin singlet state with a binding energy $k_B T_K$ at the cerium and uranium sites, which leads to a heavy fermion state with an extremely large effective mass at temperatures lower than the Kondo temperature T_K. The Kondo effect is characterized by the Kondo temperature T_K, which depends exponentially on $|J_{CF}|$ as follows:

$$T_K \propto e^{-1/(D(\varepsilon_F)|J_{CF}|)}. \tag{2}$$

The competition between the RKKY interaction and the Kondo effect was discussed by Doniach [4] as a function of $|J_{CF}|D(\varepsilon_F)$, as shown schematically in Fig. 1(a).

The magnetic susceptibility of $CeCu_6$ and $CeRu_2Si_2$ as well as that of UPt_3 and UPd_2Al_3, shown in Fig. 2, increase with decreasing temperature, following the Curie-Weiss law at high temperatures, and has a maximum at a characteristic temperature $T_{\chi\max}$ [3]. Below $T_{\chi\max}$, the susceptibility becomes almost temperature-independent, and the *f*-electron system is changed into a new electronic state, called the heavy fermion state mentioned above. Here $T_{\chi\max}$ approximately corresponds to the Kondo temperature T_K.

The heavy fermion state in the cerium compounds is roughly understood as follows [5]. The 4*f* levels of the cerium ions are split into *J*-multiplets (*J*=7/2 and 5/2) due to the spin-orbit interaction, where the 4*f* electrons in the cerium compounds are almost localized in nature. The sixfold *J*=5/2 multiplet is furthermore split into three doublets in the non-cubic crystalline electric field (CEF) scheme. The magnetic susceptibility at high temperatures follows the Curie-Weiss law with the effective magnetic moment of Ce^{3+}, namely, $2.5\mu_B$/Ce. The electronic state is, however, changed with decreasing temperature. At low temperatures, the magnetic entropy of the ground-state doublet in the 4*f* levels, *R*log2, is obtained by integrating the magnetic specific heat C_m in the form of C_m/T over the temperature. When C_m is changed into the electronic specific heat γT via the many-body Kondo effect, the following relations are obtained:

$$R\log 2 = \int_0^{T_K} \frac{C_m}{T} dT, \tag{3}$$

$$C_m = \gamma T \tag{4}$$

The γ value can be obtained as

$$\gamma = \frac{R\log 2}{T_K} \approx \frac{10^4}{T_K}\left(mJ/K^2 mol\right). \tag{5}$$

For example, the γ value and the Kondo temperature are 1600 mJ/K^{2}mol and 5 K in $CeCu_6$, and 350 mJ/K^{2}mol and 20 K in $CeRu_2Si_2$, respectively. The localized 4*f* electronic state is thus changed into an *f*-derived band with a flat energy vs momentum dispersion, possessing an extremely large effective mass. The 4*f*-itinerant band model is highly applicable to the Fermi surfaces in $CeRu_2$, $CeSn_3$ and $CeRu_2Si_2$, which are determined from the de Haas-van Alphen (dHvA) experiment, although the detected cyclotron mass m_c^* is larger than the corresponding band mass m_b. This is because the many-body Kondo effect is not included in the conventional band calculation. A similar feature is found in uranium compounds such as UPt_3 and UPd_2Al_3.

These strongly correlated electrons follow the Fermi liquid nature at low temperatures. The electrical resistivity ρ varies as $\rho = \rho_0 + AT^2$, where ρ_0 is the residual resistivity. The coefficient $\sqrt{A}$ is two to three orders of magnitude larger than that in the usual *s* and *p* electron systems. $\sqrt{A}$ correlates with an enhanced Pauli susceptibility $\chi\ (T\to 0) \approx \chi_0$ and with a large electronic specific heat coefficient $C/T\ (T\to 0) \approx \gamma$.

Interestingly, some heavy fermion systems show unconventional (anisotropic) superconductivity [6]. The most important observation for the well-known heavy fermion superconductors such as $CeCu_2Si_2$, UPt_3, and UPd_2Al_3 is that superconductivity is realized in the magnetically ordered state or the antiferromagnetic (ferromagnetic) fluctuations. The physical quantities such as the specific heat and the spin-lattice relaxation rate do not follow the exponential dependence of $e^{-\Delta/k_B T}$ in the

superconducting state, which is expected from Bardeen-Cooper-Schrieffer (BCS) theory, but obey a power law of T^n. Here, Δ is the superconducting energy gap and n is an integer. This means that the superconducting gap possesses line and/or point nodes. These results are based on the fact that quasi-particles with heavy masses of 10-100m_0 (m_0: rest mass of an electron) are of an *f* electron character, which originates from the strong Coulomb repulsion between the *f* electrons. These quasi-particles condense into Cooper pairs.

When the phonon-mediated attractive interaction is compared with the strong repulsive interaction among the *f* electrons, it is theoretically difficult for the former interaction to overcome the latter. To avoid a large overlap of the wave functions of the paired particles, the heavy-fermion system preferentially chooses an anisotropic channel, such as a *p*-wave spin triplet state or a *d*-wave spin singlet state to form Cooper pairs [6]. Recent neutron-scattering experiments clearly indicated evidence of a close relationship between superconductivity and magnetic excitation in UPd_2Al_3 [7-9]. The magnetic excitation gap of UPd_2Al_3, which appears in the inelastic neutron profile below the superconducting transition temperature T_{SC}, corresponds to the superconducting order parameter.

Figure 3 shows a schematic view of the superconducting order parameter with *s*-, *d*-, and *p*-wave pairing. The order parameter $\Psi(r)$ with even parity (*s*- and *d*-waves) is symmetric with respect to *r*, where one electron with the up-spin state of the Cooper pair is simply considered to be located at the center of $\Psi(r)$, where r=0, and the other electron with the down-spin state is located at *r*. The width of $\Psi(r)$ with respect to *r* is called the coherence length ξ, as shown in Fig 3(a).

The technique of nuclear magnetic resonance (NMR) and nuclear quadrupole resonance (NQR) has proved to be a useful tool for determining the symmetry of the superconducting condensate. UPd_2Al_3 is considered to be a *d*-wave superconductor from NMR experiments [10], which corresponds to the case in Fig. 3(b). The origin of pairing has also been clarified by neutron-scattering experiments on UPd_2Al_3 [7-9], as mentioned above. On the other hand, $\Psi(r)$ with odd parity (*p*-wave) is not symmetric with respect to *r*, where the parallel spin state is shown in Fig. 3(c). From NMR and magnetization experiments [11, 12], UPt_3 is considered to possess odd parity in symmetry.

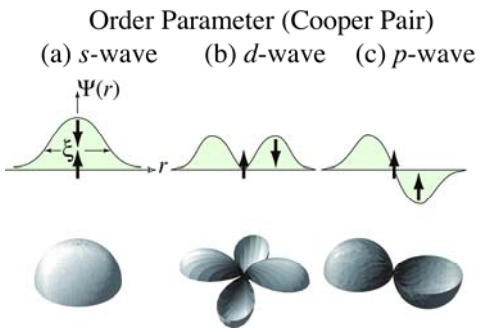

Fig. 3. Schematic view of the superconducting order parameter with s-wave, d-wave and p-wave pairing.

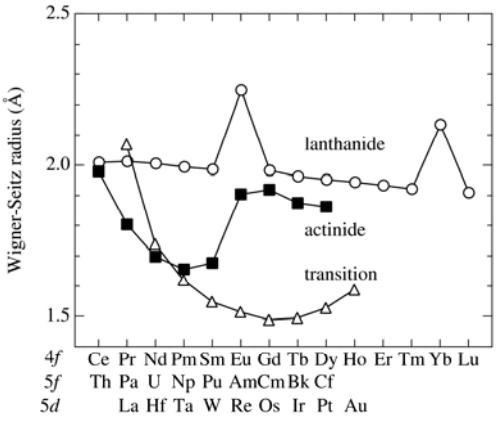

Fig. 4. Wigner-Seitz radius of the actinide, lanthanide and transition metals [18].

Recently, a new aspect of cerium and uranium compounds with magnetic ordering has been discovered. When pressure *P* is applied to compounds with antiferromagnetic ordering such as $CeCu_2Ge_2$ [13], $CeIn_3$, and $CePd_2Si_2$ [14], the Néel temperature T_N reaches zero at the quantum critical pressure P_C, and superconductivity is observed at around P_C. Superconductivity is surprisingly found even in the ferromagnetic states of UGe_2 [15], URhGe [16], and UIr [17]. The crossover from the magnetically ordered state to the non-magnetic state under pressure, crossing the quantum critical point, is the most interesting issue in strongly correlated *f* electron systems. The electronic states can be tuned by pressure. Experimentally, the quantity $|J_{CF}|D(\varepsilon_F)$ in Fig. 1(a) corresponds to pressure *P*.

It is also noted that the wave function of *f* electrons in the rare earths and actinide metals shrinks with increasing the number of *f* elements. In the rare earths, this corresponds to the lanthanide contraction. There exists the similar trend for the actinide metals such as Th, Am, Cm, Bk and Cf, revealing the localized nature of *f* electrons. On the other hand, the Wigner-Seitz radius R_{WS}, which is related to the atomic volume V $\left(=(4\pi/3)R_{WS}^3\right)$, steeply decreases from Th to Np, as in transition metals, but increases as a function of the number of 5*f* electrons, as shown in Fig. 4 [18]. The Wigner-Seitz radius of Am is close to the localized 4*f*-electron radius of lanthanide metals, and thus the radius of Pu has an intermediate value between Np and Am. This is an important feature to understand the electronic states of actinide compounds, which is also related to the crystal structure.

The 5*f*-itinerant band model is applicable to the electronic state of a heavy-fermion superconductor UPt_3, as noted above. On the other hand, the 5*f*-localized electronic state is also well established experimentally in UPd. The electronic states in transuranium compounds including Np and Pu are still to be clarified, both experimentally and theoretically [19].

In the next chapter, we present several kinds of

techniques for growing high-quality single crystals of rare earth and actinide compounds, and describe the dHvA effect. We explain in Chap. 3 the characteristic features of heavy fermions, namely the meaning of heavy fermions and the metamagnetic transition in the magnetization curve. We furthermore present the Fermi surface properties based on the results of de Haas-van Alphen (dHvA) experiment and energy band calculation in RX_3 (AnX_3) and RTX_5 ($AnTX_5$) (R: rare earth, An: actinide, T: transition metal, X: Al, Ga, In, Si, Ge, Sn, Pb) and *f*-relevant superconductivity in Chap. 4. In the final chapter, the characteristic features in these compounds are summarized.

2. Single crystal growth and dHvA experiment

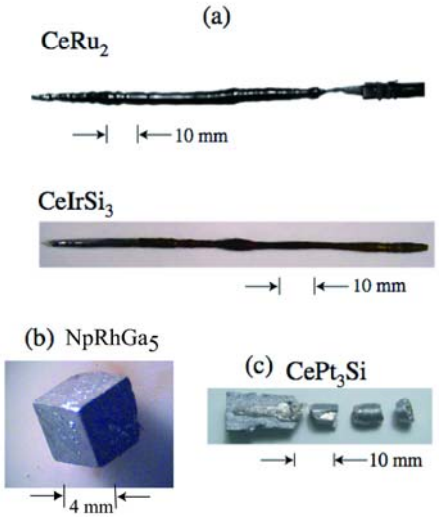

Fig. 5. Photograph of single crystal ingots obtained by (a) Czochralski, (b) flux and (c) Bridgman methods.

In the dHvA experiment, we need high-quality single crystals as well as low temperatures down to 30 mK and strong magnetic fields up to 170 kOe. Various techniques for the single crystal growth were applied to rare earth and actinide compounds, depending on the degree of the vapor pressure of the melt, as shown in Tables 1-4 for cerium, thorium, uranium and transuranium compounds, respectively [20]. These compounds were used for the dHvA experiment. If the vapor pressure is low, the Czochralski method denoted as Cz is a powerful method to obtain a large size of a single crystal ingot. The rf-furnace was used for the Cz method when the melting point is less than 1500°C and the tungsten crucible is available. The Cz method was also applied to the compounds with high-melting points, for example about 2500°C, in the tetra-arc furnace. The typical compounds with high-melting points are $CeRh_3B_2$, UB_2 and UC. Figure 5(a) shows single crystal ingots of $CeRu_2$ and $CeIrSi_3$ grown by the Cz method in the tetra-arc furnace. $CeIrSi_3$ is known to be a pressure-induced superconductor without inversion symmetry in the tetragonal crystal structure [21]. On the other hand, the flux method (Flux), the chemical transport method (CT) and the Bridgman method (Br) are useful in the high vapor pressure case of the compounds, and also for the incongruent compounds. The floating zone method (FZ) was also applied to CeB_6. Figure 5(b) indicates a single crystal of $NpRhGa_5$ grown by the Ga-flux method, where the Fermi surface properties are described later. A single crystal of $CePt_3Si$ was grown by the Br method in a Mo-crucible, as shown in Fig. 5(c).

It is noted that the starting material of a uranium ingot was annealed under high vacuum of 10^{-10} torr via the solid state electrotransport method. For example, an Fe impurity of 40 ppm in the uranium ingot was reduced to less than 2 ppm, and the Cu impurity was completely removed [22]. Subsequent annealing under high vacuum using the electrotransport method drastically improved the quality of the single crystal, which was applied to UPt_3 and URu_2Si_2. For example, we recently obtained an extremely high-quality single crystal sample in URu_2Si_2, where the residual resistivity ratio (RRR) reaches more than 500 [19].

Table 1. Single crystal growth and Fermi surface studies in cerium compounds.

Cz	$CeRu_2$(P) $CeRh_2$(P) $CeSn_3$(P) CeNi(P) $CeRu_2Si_2$(P) CeAg(Q,F) $CeGa_2$(F) $CeRh_2B_2$(F) $CeRu_2Ge_2$(F) CePtAl(F) $CeIn_3$(AF) Ce_2Sn_7(AF) $CeRh_2Si_2$(AF)
Flux	$CeIrIn_5$(P) $CeCoIn_5$(P) $CeAgSb_2$(F) $CeRhIn_5$(AF) $CeGoGe_3$(AF) Ce_2RhIn_8(AF)
Br	CeSb(AF) $CePt_3Si$(AF,S) CePtP(AF) CePtAs(AF)
FZ	CeB_6(Q, AF)

Table 2. Single crystal growth and Fermi surface studies in thorium compounds.

Flux	$ThIn_3$(P) $ThRhIn_5$(P)

Table 3. Single crystal growth and Fermi surface studies in uranium compounds.

Cz	UC(P) USi_3(P) UB_2(P) UB_4(P) UPt_3 (P,S) URu_2Si_2 (S) UGe_2(F) UIr (F) UPd_2Al_3(AF,S)
Flux	UAl_3(P) $UfeGa_5$(P) $UcoGa_5$(P) $UrhGa_5$(P) UGa_2(F) UGa_3(AF) UIn_3(AF) USb_2(AF) UBi_2(AF) $UniGa_5$(AF) $UPdGa_5$(AF) $UptGa_5$(AF)
CT	U_3P_4 (F) U_3As_4 (F) UP_2(AF) UAs_2(AF)

Table 4. Single crystal growth and Fermi surface studies in transuranium compounds.

Flux	$NpGe_3$(P) $NpNiGa_5$(AF) $NpCoGa_5$(AF) $NpRhGa_5$ (Q,AF) $NpPtGa_5$(AF) $PuIn_3$(P)

The dHvA experiment was performed by the standard field-modulation method with a modulation frequency of 7 Hz and a modulation field of 100 Oe [1, 2]. Pressure was applied up to 3 GPa using an MP35N piston-cylinder cell with a 1:2 mixture of commercial Daphne oil (7373) and petroleum ether as a pressure-transmitting medium. The pressure was calibrated by the T_{sc} value of Sn, which is accurate within 0.05 GPa of the absolute value.

The detected dHvA signal in the 2ω technique is written as follows [23]:

$$V_{OSC} = \sum_p A_p \sin\left(\frac{2\pi pF}{H} + \phi_p\right) \tag{6}$$

$$A_p \propto J_2\left(\frac{2\pi Fh}{H^2}\right) H^{1/2} p^{-3/2} \left|\frac{\partial^2 S_F(k_z)}{\partial k_z^2}\right|^{-1/2} R_T R_D R_S \tag{7}$$

$$R_T = \frac{2\alpha m_c^* T / H}{\sinh\left(2\alpha m_c^* T / H\right)} \tag{8}$$

$$R_D = \exp\left(-\alpha m_c^* T_D / H\right) \tag{9}$$

$$R_S = \cos\left(p\pi m_c^* g / 2m_0\right) \tag{10}$$

$$\alpha = 2\pi^2 pck_B / e\hbar \tag{11}$$

Index p (=1, 2, 3, ...) represents the fundamental (p=1) and the higher-harmonic (p=2,3,...) dHvA frequencies, and J_2 is the Bessel function. The dHvA amplitude is related to the so-called curvature factor $\partial^2 S_F(k_z)/\partial k_z^2$, the thermal reduction factor R_T ($R_T \to 1$ for $T \to 0$), the Dingle reduction factor R_D ($R_D \to 1$ for the Dingle temperature $T_D \to 0$), which is caused by the finite scattering lifetime of the conduction electrons, and the spin reduction factor R_S ($R_S \to 1$ for the cyclotron mass $m_c^* = m_0$ and g= 2), which is the interference between the oscillations of spin-up and spin-down electrons. The dHvA frequency $F(= c\hbar S_F / 2\pi e)$ is proportional to the extremal (maximum or minimum) cross-sectional area S_F of the Fermi surface. From the temperature and field dependences of the dHvA amplitude, we can determine the cyclotron effective mass m_c^* and the Dingle temperature T_D, respectively. $T_D(= \hbar / 2\pi k_B \tau)$ is inversely proportional to the scattering lifetime τ of an conduction electron. We also estimate the mean free path ℓ from the simple relations: $S_F = \pi k_F^2$, $\hbar k_F = m_c^* v_F$ and $l = v_F \tau$, where k_F is half of the caliper dimension of a circular S_F and v_F is the Fermi velocity.

The experimentally obtained dHvA results of cerium, thorium, uranium and transuranium compounds, which are shown in Tables 1-4, respectively, were compared with the results of energy band calculation [1-3, 19, 21, 24-26]. These compounds include a wide variety of electronic states such as paramagnetism including Pauli paramagnetism, denoted as (P) in Tables 1-4, quadrupolar ordering (Q) including the multi-polar ordering, ferromagnetism (F), antiferromagnetism (AF) and superconductivity (S).

3. Characteristic features of heavy fermions

First we show an example of how the heavy fermions are formed. The uranium compounds UX_3 with the cubic $AuCu_3$ type structure exhibit a wide variety of magnetic properties such as Pauli paramagnetism in USi_3 and UGe_3, spin fluctuations in USn_3 and UAl_3 and antiferromagnetism in Upb3, UGa_3, UIn_3 and UTl_3 [27, 28]. The variety in the magnetic properties is closely related to the lattice constant or the distance between the U atoms, $d_{U\text{-}U}$, and the 5*f*-electron hybridization with the other valence electrons. This is reflected in the electronic specific heat coefficient γ, which varies from 14 mJ/K^{2}mol in USi_3 to 170 mJ/K^{2}mol in USn_3, as shown in Fig. 1(b). When the antiferromagnetic order occurs at T_N=30 K in UPb_3, the γ value is reduced to 110 mJ/K^{2}mol. The γ value in UX_3 thus depends on the lattice constant, $d_{U\text{-}U}$. It can be deduced from Fig. 1(b) that as $d_{U\text{-}U}$ becomes shorter, the 5*f* bands become wider, enhancing Pauli itinerancy, while with increasing the 5*f* bands become narrower, forming a heavy fermion state, as in USn_3, and finally the 5*f*-electronic state exhibits magnetic ordering [28]. The dependence of magnetism on the *f*-*f* overlap was long ago discussed by Hill [29].

A large cyclotron mass of 100 m_0 (: rest mass of an electron) was detected in the dHvA experiment: 120 m_0 in $CeRu_2Si_2$ [30], 87 m_0 in $CeCoIn_5$ [31], 105 in UPt_3 [32], 65 m_0 in UPd_2Al_3 [33] and 81 m_0 in $PrFe_4P_{12}$ [34], whereas the corresponding band mass is roughly by one order smaller than the detected cyclotron mass.

We note that the topology of the Fermi surface in $CeRu_2Si_2$, $CeCoIn_5$ and UPt_3 without a distinct magnetic ordering is well explained by the *f*-itinerant band model. The heavy fermion antiferromagnet UPd_2Al_3 with a magnetic moment of 0.85μ_B /U is also well explained by the energy band calculation based on the fully-relativistic spin-polarized LAPW method. Namely, the 5*f*-electrons in the antiferromagnetically ordered UPd_2Al_3 are itinerant and also contribute to the magnetic moment at the uranium sites.

The magnetically ordered cerium compounds are, however, different in magnetism compared to the uranium compounds. In the cerium compounds the magnetic order

is formed by the localized-4*f* moments. The topology of the Fermi surface is therefore similar to that of the corresponding non-4*f* lanthanum compound. Nevertheless, the γ value or the effective mass of the conduction electrons in the Kondo antiferromagnets such as $CeAl_2$ and CeB_6 are by one to two orders of magnitude larger than those of the corresponding non-4*f* reference compounds $LaAl_2$ and LaB_6 [35, 36]. The degree of mass enhancement depends on the degree of competition between the RKKY interaction and the Kondo effect, namely the hybridization of the 4*f* electrons with the conduction electrons.

The conduction electrons with large masses in the heavy electron systems are believed to move slowly in the crystal. We confirmed from the dHvA experiment that the product of the cyclotron mass and the inverse scattering lifetime or the Dingle temperature is constant in $CeIn_3$ [37].

The relation between the effective mass and the scattering lifetime τ for the conduction electrons in metals is defined as follows:

$$\hbar k_F = m_c^* v_F \tag{12}$$

and

$$l = v_F \tau \tag{13}$$

From eqs. (12) and (13) the following equation is obtained:

$$\frac{m_c^*}{\tau} = \frac{\hbar k_F}{2\pi k_B l} \tag{14}$$

Thus m_c^* / τ is expected to be the same for two similar orbits with the same mean free path. When the effective mass m_c^* is enhanced by a factor of (1+λ) due to the many-body Kondo effect, eq. (12) indicates that τ should also be enhanced by a factor of (1+λ). This occurs because a large mass is translated into a small velocity from eq. (13) so that the scattering lifetime becomes (1+λ) times larger than that obtained by eq. (13) if the mean free path is the same. In terms of the Dingle temperature $T_D (= \hbar / 2\pi k_B \tau)$, eq. (14) becomes

$$m_c^* T_D = \frac{\hbar k_F}{2\pi k_B l} \tag{15}$$

The above relation between the cyclotron mass and the Dingle temperature was applied to the heavy electrons in $CeIn_3$ [37]. There are two orbits, named orbits d and D, which possess the same dHvA frequency in $CeIn_3$ and therefore the same cross-sectional area of the Fermi surface but a different cyclotron mass for two field directions for the same nearly spherical Fermi surface, as later shown in Fig. 19(c). Thus, $\hbar k_F$ is the same for the two orbits. Moreover, the mean free path is considered to be the same because it is approximately equal to the average distance between impurities.

The dHvA frequency *F*, which is proportional to , and the cyclotron mass, which is determined from the temperature dependence of the dHvA amplitude for the field along the ⟨111⟩ direction, are 3.15×10^7 Oe and 2.44 m_0 respectively, for orbit d . The other orbit for field approximately along the ⟨110⟩ direction, which is now denoted by orbit D, has 3.29×10^7 Oe and 12 m_0. Here the cyclotron masses were determined from the temperature dependence of the dHvA amplitude *A*.

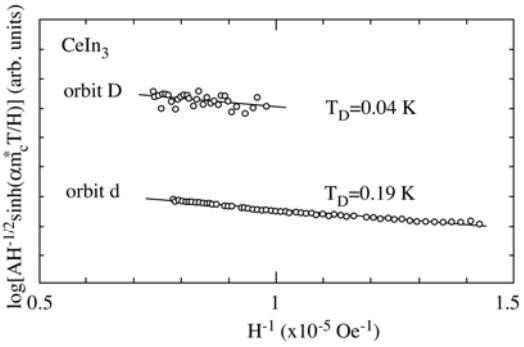

Fig. 6. Dingle plot for orbits d and D of the same Fermi surface in $CeIn_3$.

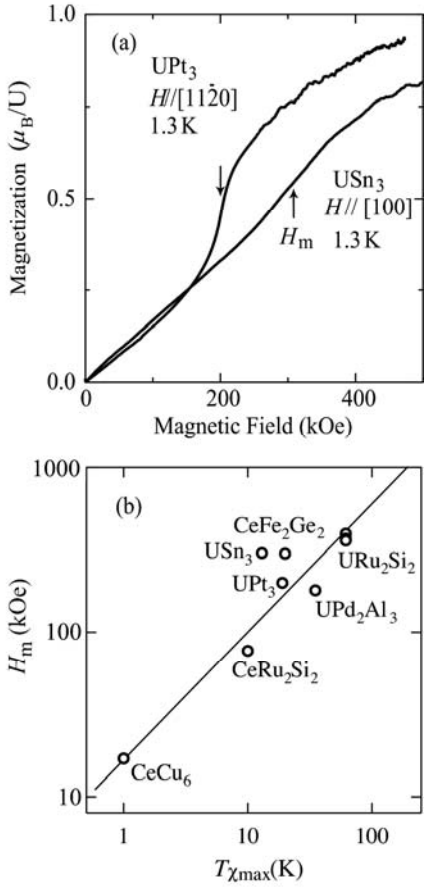

Fig. 7. (a) Metamagnetic transition in UPt_3 and USn_3, and (b) H_m vs. $T_{\chi\max}$ in heavy fermions of cerium and uranium compounds.

Fig. 6 shows a Dingle plot of log $[AH^{-1/2}\sinh(\alpha m_c^* T/H]$ vs H^{-1} for these two orbits. The slope in Fig. 6 gives the product of the cyclotron mass m_c^* and the Dingle temperature T_D. A slope for orbit d is almost the same as that for orbit D, indicating that the product of is constant for the two orbits. Orbit d possesses T_D=0.19 K or $\tau=6.5\times10^{-12}$s, while T_D=0.04 K or $\tau=3.0\times10^{-11}$ s for orbit D.

We can thus conclude that the larger the mass becomes, the larger the scattering lifetime, keeping the value of $m_c^*\tau^{-1}$ or $m_c^* T_D$ constant.

The metamagnetic transition in the magnetization curve is one of the important characteristics in the heavy fermion compounds. As noted above, the heavy fermion state is formed due to the hybridization effect between the conduction electrons with a wide energy band and almost localized *f*-electrons. As a consequence, the almost localized *f*-electrons become itinerant with decreasing temperature through the many-body Kondo effect. The crossover from localized to itinerant occurs at a characteristic temperature $T_{\chi\max}$, where the magnetic susceptibility has a maximum, as mentioned above. $T_{\chi\max}$ corresponds approximately to the Kondo temperature , which is about 20 K in $CeRu_2Si_2$, for example, as shown in Fig. 2. At temperatures lower than $T_{\chi\max}$, the metamagnetic transition occurs at a magnetic field H_m such that $k_B T_{\chi\max} \approx g_{eff}\mu_B H_m$. Figure 7(a) shows the typical metamagnetic transition in UPt_3 and USn_3, which occurs at H_m = 200 kOe and 310 kOe, respectively [28]. The relation of H_m vs $T_{\chi\max}$ in cerium and uranium compounds is shown in Fig. 7(b) [38].

H_m is thus a characteristic field. The field dependence of the specific heat has a maximum at H_m [39, 40]. For $H > H_m$, the cyclotron mass decreases with increasing field. The mass reduction at high fields is also a characteristic feature in heavy fermions, which is shown later for $CeCoIn_5$ in Fig. 51.

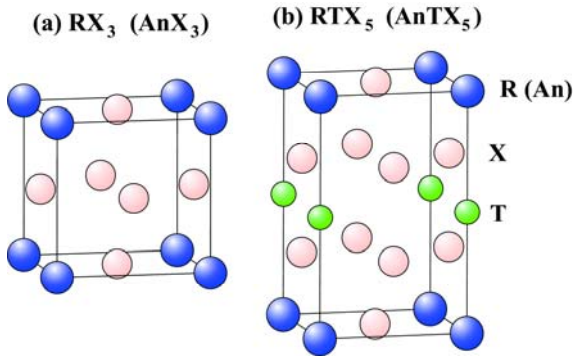

Fig. 8. (a) Cubic crystal structure in RX_3 and AnX_3 and (b) the tetragonal structure in RTX_5 and $AnTX_5$.

4 . Changes of the electronic states in the RX_3 and AnX_3 compounds with the cubic crystal structure and the RTX_5 and $AnTX_5$ compounds with the tetragonal crystal structure

4.1 RX_3 and AnX_3

The cubic RX_3 and AnX_3 compounds in Fig. 8(a) are classified in Table 5 according to the number of valence electrons, *n*, from *n*=11 in a divalent Yb^{2+} compound of YbIn to *n*=19 in a 5*f*-relevant paramagnet $NpGe_3$, passing through a non-4*f* reference compound $LaIn_3$ ($LuIn_3$), an antiferromagnet $NdIn_3$, a Kondo-lattice compound with antiferromagnetic ordering $CeIn_3$, $CeIn_3$ under pressure, another reference compound $ThIn_3$, another divalent Yb^{2+} compound of $YbPb_3$, another non-4*f* reference compound $LaSn3_3$, a heavy fermion compound UAl_3, antiferromagnets UGa_3 and Uin_3, an itinerant-4*f* compound $CeSn_3$, a Pauli paramagnet USi_3 (UGe_3), a spin-fluctuation compound USn3, an antiferromagnet $NpIn_3$, and a paramagnet $PuIn_3$.

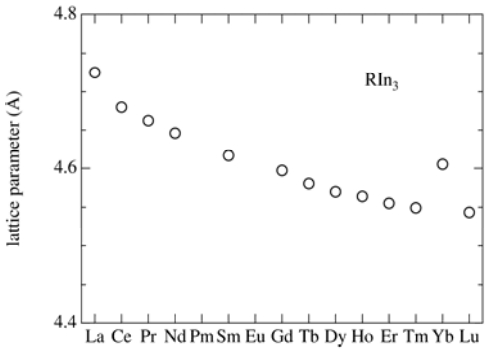

Fig. 9. Lattice parameter in RIn_3 with the cubic structure [41].

$YbIn_3$ in Table 5 is a Pauli paramagnet with the divalent property of Yb^{2+}. This is clear from the lattice constant in RIn_3, as shown in Fig. 9, because the lattice constant of YbIn deviates from the lanthanide contraction [41]. The electronic configuration of the Yb atom is $4f^{14}5s^25p^66s^2$, and thus the valence electrons are $6s^2$. Considering the valence electrons of $5s^25p^1$ in the In atom, the total number of valence electrons are 11 in $YbIn_3$, revealing an uncompensated metal. Figure 10 shows the angular dependence of the dHvA frequency in $YbIn_3$ [42]. The solid lines in Fig. 10 indicate the results of energy band calculation. The experimental results of dHvA branches named α, β, γ, δ_i and ε are in good agreement with the theoretical ones, as shown in Fig. 11, which are the band 6-electron Fermi surface centered at R, the band 7-electron Fermi surface centered at R, the band 6-electron Fermi surface centered at Γ, the band 5-hole Fermi surface centered at M and band 5-hole located along Λ, respectively. Branch ζ also corresponds to the band 6-

electron Fermi surface. The cyclotron mass is light and is close to the corresponding band mass m_b , ranging from 1.1 m_0 in branch α to 0.22 m_0 in branch ζ.

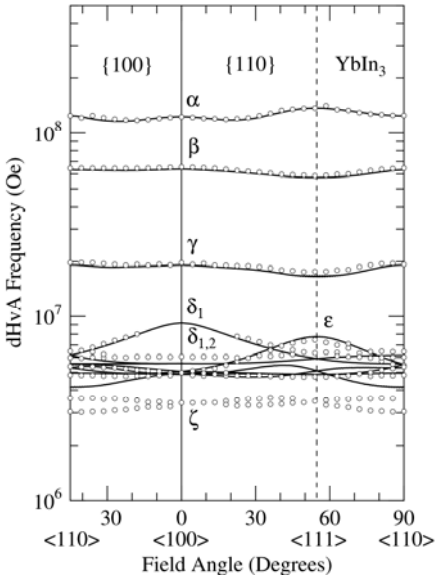

Fig. 10. Angular dependence of the dHvA frequency in a Pauli paramagnet $YbIn_3$. The solid lines are the results of energy band calculation.

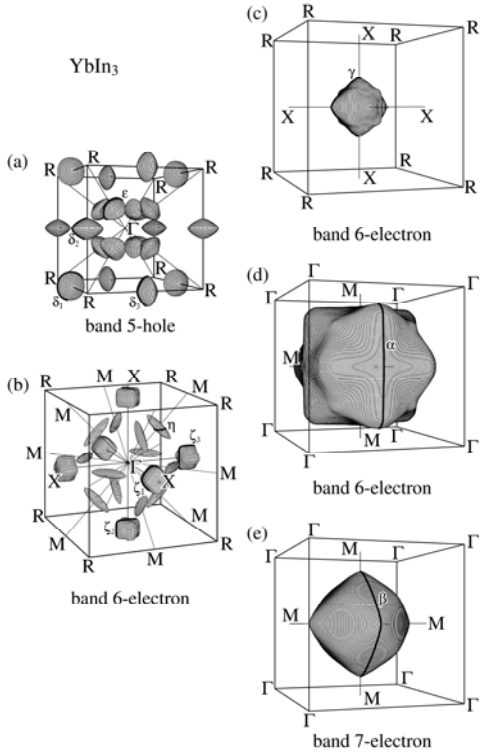

Fig. 11. Theoretical Fermi surfaces in a Pauli paramagnet $YbIn_3$.

Table 5. Numbers of valence electrons and Fermi surface studies in the RX_3 and AnX_3 compounds with the $AuCu_3$-type cubic crystal structure.

Number of valence Electrons	Compounds	refs
11	$YbIn_3$	[42]
12	$LaIn_3$ $LuIn_3$ $NdIn_3$ (AF) $CeIn_3$ (AF) $NpIn_3$ (AF)	[42][43][45] [46][50][69]
13	$CeIn_3$ under pressure $ThIn_3$	[51][52]
14	$YbSn_3$ $YbPb_3$	[55][56]
15	$LaSn_3$ UAl_3 UGa_3(AF) Uin_3 (AF)	[57][62] [64][65]
16	$CeSn_3$	[59]
17	$PuIn_3$	[71]
18	USi_3 UGe_3 USn_3	[66][67]
19	$NpGe_3$	[68]

Next we show in Fig. 12(a) the angular dependence of the dHvA frequency in $LaIn_3$ [43]. The solid lines represent the results of energy band calculation [44]. Branch "*a*" originates from the band 7-electron Fermi surface with the nearly spherical topology, while the others originate from the band 6-hole Fermi surface, as shown in Fig. 13. $LaIn_3$ is a compensated metal with equal number of electrons and holes, or equal volume of the electron Fermi surface and the hole Fermi surface. The latter Fermi surface consists of three kinds of major parts. Among them, a Fermi surface centered at Γ, denoted by "*d*", is electron in dispersion and is spherical in topology, bulges slightly along the <1 0 0> direction and connects with another part of the Fermi surface centered at R by a slender arm elongated along the <1 1 1> direction. The arm is denoted by "*j*". The topology of the Fermi surface for branch "*d*" is similar to that of Cu, although the volume is small compared to that of Cu.

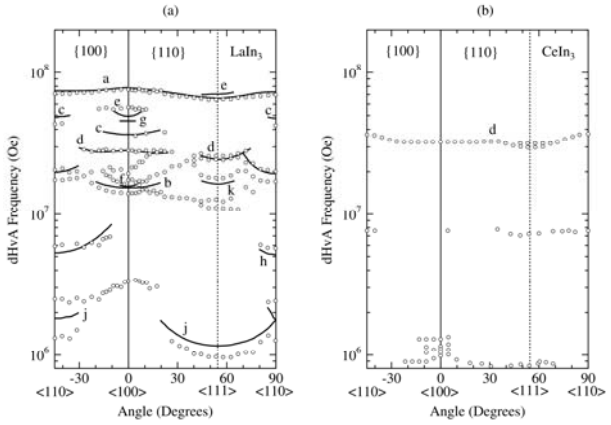

Fig. 12. Angular dependence of the dHvA frequency in (a) $LaIn_3$ and (b) $CeIn_3$. The solid lines in (a) are the results of band calculations.

Conduction electrons are mainly due to La 5*d* and In 5*p* electrons. The cyclotron masses for branches *a* and *d* for $H \| <100>$ are 0.57 m_0 and 0.40 m_0, respectively, which are almost the same as the corresponding band masses of 0.58 m_0 and 0.53 m_0, respectively.

Next we consider a change of the Fermi surface in the antiferromagnetic state of NdIn with a Néel temperature T_N = 5.9K [45, 46]. The magnetic structure in the antiferromagnetic state with a magnetic wave vector q=(1/2, 0, 1/2), determined by the neutron scattering experiment, is tetragonal, as shown in Fig. 14 [47].

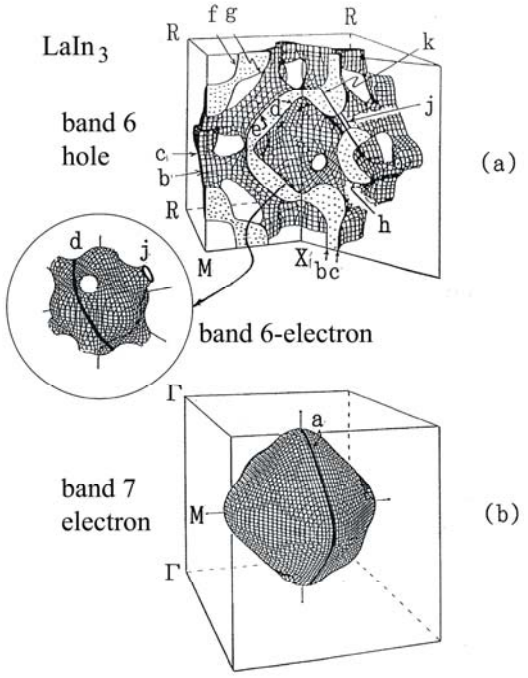

Fig. 13. (a) Band 6-hole and (b) band 7-electron Fermi surfaces in $LaIn_3$.

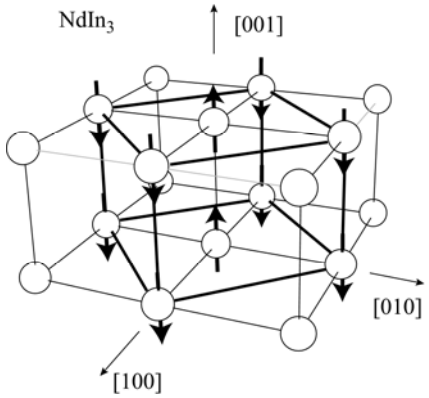

Fig. 14. Antiferromagnetic structure in $NdIn_3$. Four chemical unit cells are shown, where one magnetic unit cell is represented by thick solid lines with arrows indicating the directions of the magnetic moments.

Fig. 15 shows the magnetization curve with three metamagnetic transitions at 78.2, 88.5 and 111.4 kOe, which are indicated by the vertical broken lines [48], and the dHvA oscillation for H || <1 0 0>. With increasing magnetic field, the compound changes from the antiferromagnetic state to a field-induced ferromagnetic (or paramagnetic) state, passing through an intermediate-magnetic state. The FFT spectrum in $NdIn_3$ is roughly the same as the one in $LaIn_3$ because the 4*f* electrons in $NdIn_3$ are localized and therefore do not contribute to the volume of the Fermi surface. Among the dHvA branches in the antiferromagnetic state of NdIn, we remark branch "*a*" due to the band 7-electron Fermi surface. Figure 16 shows the field dependence of the dHvA frequency of branch "*a*". The dHvA frequency corresponding to the up- and down-spin states of the conduction electrons is degenerated in the antiferromagnetic state, and also in the intermediated-magnetic state, while it is split into the up- and down-spin states in the field-induced ferromagnetic (paramagnetic) state.

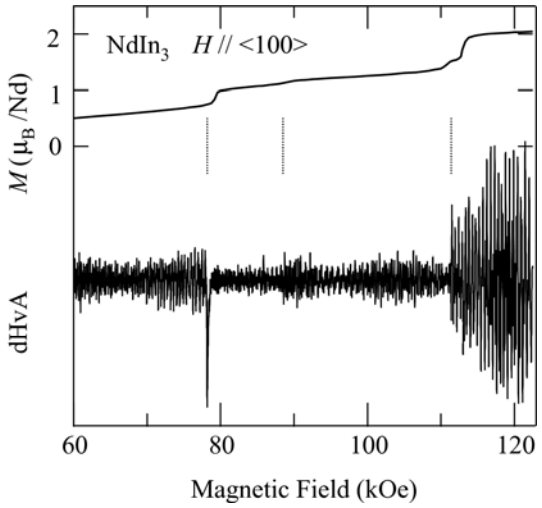

Fig. 15. Magnetization curve and the dHvA oscillation for H || <1 0 0> in $NdIn_3$. The data of magnetization curve are cited from ref.[48].

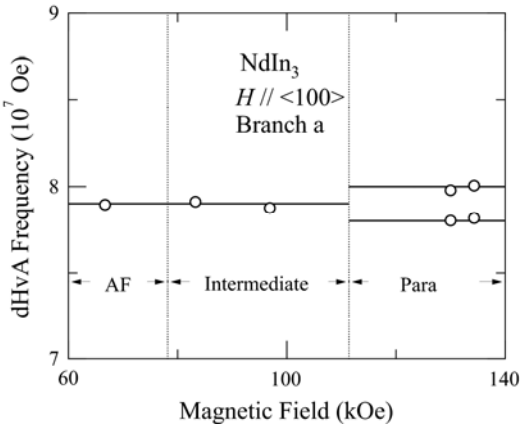

Fig. 16. Field dependence of the dHvA frequency in $NdIn_3$.

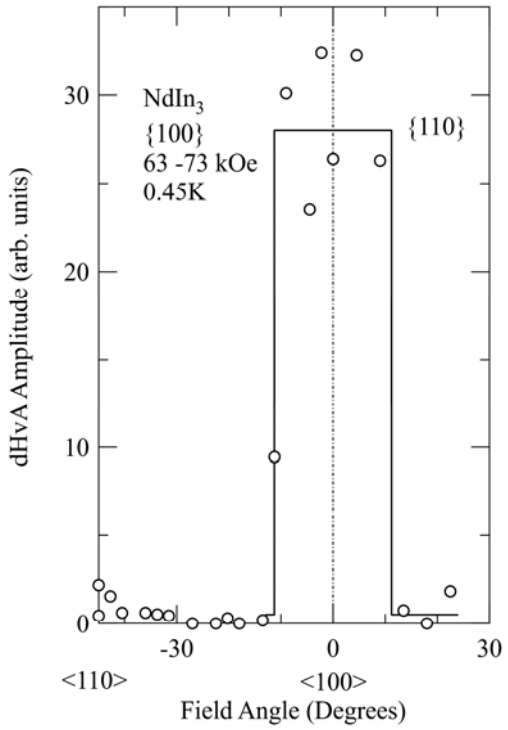

Fig. 17. Angular dependence of the dHvA amplitude for branch "a" in $NdIn_3$.

It is noticed that the dHvA amplitude of branch "*a*" strongly depends on the field direction, as shown in Fig. 17. This is due to the small magnetic Brillouin zone based on the large tetragonal magnetic structure shown in Fig. 14. From the angular dependence of the dHvA amplitude for branch "*a*", the nearly spherical electron-Fermi surface in the paramagnetic state of $NdIn_3$, as shown in Fig. 13(b) or Fig. 18(a), which corresponds to branch "*a*" in $LaIn_3$, is changed into a multiply-connected Fermi surface with necks in the antiferromagnetic state, as shown in Fig. 18(b). Note that no necks exist along the [1 0 0] and [0 1 0] directions. Therefore, the cubic symmetry is broken in the antiferromagnetic state. If we follow the Fermi surface in Fig. 18(b), branch "*a*" is not detectable for $H \,||< 110 >$, but is experimentally detected even in the antiferromagnetic state, although its amplitude is extremely small, as shown in Fig. 17. This is because an electron can circulate along a closed orbit by breaking through the necks of the Fermi surface. The antiferromagnetic Fermi surface in the 4*f*-localized antiferromagnet NdIn is thus reconstructed on the basis of the magnetic Brillouin zone.

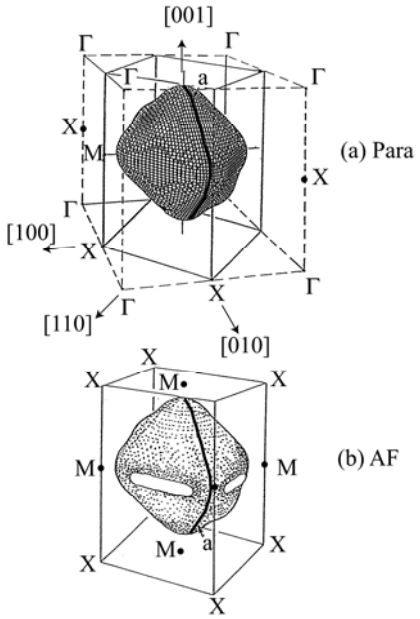

Fig. 18. Fermi surfaces in (a) the paramagnetic state and (b) the antiferromagnetic state in $NdIn_3$.

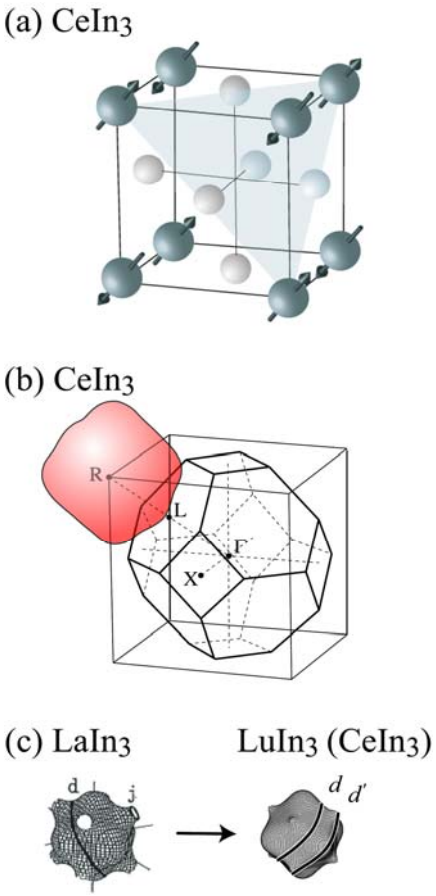

Fig. 19. (a) Crystal and magnetic structure in $CeIn_3$, (b) the magnetic Brillouin zone of $CeIn_3$ and (c) Fermi surfaces in LaIn and $LuIn_3$ ($CeIn_3$).

The similar change of the electronic state due to the magnetic structure is realized in a Kondo-lattice compound CeIn with antiferromagnetic ordering at T_N = 10 K, where ordered moments of 0.5μ_B /Ce with the propagation vector q = (1/2, 1/2, 1/2) are aligned along the <1 1 1> direction as shown in Fig. 19(a) [49]. The angular dependence of the dHvA frequency in CeIn is shown in Fig. 12(b) [50]. The detected dHvA named "*d*" in CeIn is very close to the one in $LaIn_3$. Branch "*d*" in $CeIn_3$ is, however, observed in the whole angle region, possessing no arms, indicating that the Fermi surface is a nearly spherical Fermi surface with humps, because in another non-4*f* ($4f^{14}$) reference compound $LuIn_3$, there exist no necks [42].

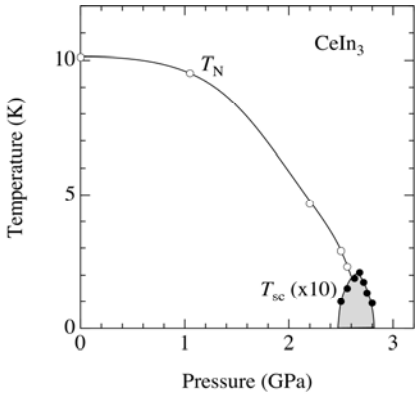

Fig. 20. Phase diagram for the Néel temperature T_N and the superconducting transition temperature T_{SC} in $CeIn_3$.

Branch "*a*" is, however, not detected in $CeIn_3$, which is ascribed to the reconstruction of the Fermi surface on the basis of the antiferromagnetic Brillouin zone. This Brillouin zone is the same as that for the face-centered cubic structure, as shown in Fig. 19(b). Most of the band 7-electron Fermi surface centered at the R point is changed into a fully occupied band in this new Brillouin zone, where the original R point is reduced to the Γ point in this Brillouin zone.

A drastic change of the Fermi surface in an antiferromagnetic Kondo compound $CeIn_3$ is realized under pressure [51]. The dHvA experiment was carried out under pressure. With increasing pressure P, the Néel temperature decreases as a function of pressure and becomes zero at $P_c \approx$ 2.60 GPa, together with an appearance of superconductivity (the superconducting transition temperature T_{sc}= 0.2 K) in the pressure region from 2.50 to 2.81 GPa, as shown in Fig. 20.

Fig. 21 shows the pressure dependence of the dHvA frequency for $H \parallel$ <1 0 0>. A large main Fermi surface named "*a*" is observed in the pressure region $P > P_c \approx 2.60$ GPa. The dHvA frequency Oe at 2.7 GPa is , however, larger than F=9.87 x 10^7 Oe in LaIn, but is close to F=7.47 x 10^7 Oe in $ThIn_3$ [52]. A Pauli paramagnet ThIn with the tetra-valence electrons ($6d^27s^2$) of the thorium atom is another kind of a good reference compound to investigate the topology of the 4*f*-itinerant Fermi surface in $CeIn_3$ with the tetra-valence electrons ($4f^15d^16s^2$) of cerium.

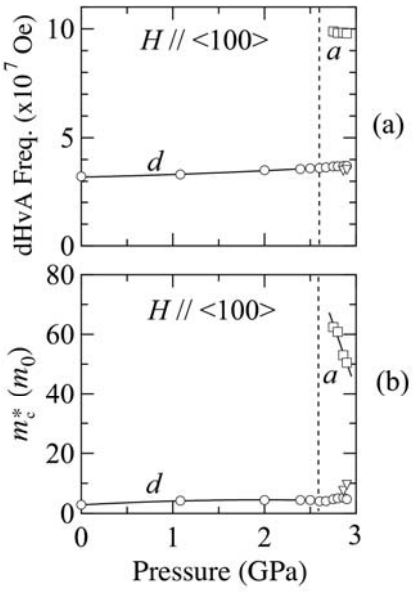

Fig. 21. Pressure dependence of the dHvA frequency and the cyclotron mass for $H \parallel$ <1 0 0> in $CeIn_3$.

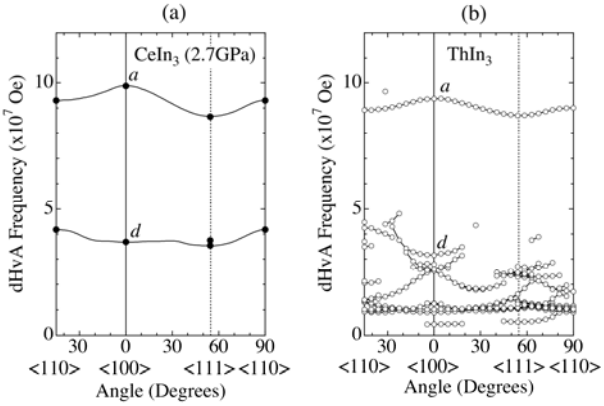

Fig. 22. Angular dependence of the dHvA frequency in (a) $CeIn_3$ at 2.7 GPa and (b) $ThIn_3$.

We show in Fig. 22 the angular dependence of the dHvA frequency in $CeIn_3$ at 2.7 GPa and $ThIn_3$. The large nearly spherical Fermi surface at 2.7 GPa in $CeIn_3$ corresponds to the band 7-electron Fermi surface centered at the R point, on the basis of the 4*f*-itinerant band model, as shown in Fig. 23. Namely, the band 6-hole Fermi surface in $LaIn_3$ is completely occupied by the electron, and the band 7-electron Fermi surface is changed into the enlarged spherical Fermi surface centered at R and a complicated multiply-connected electron Fermi surface centered at Γ in the band 7-electron Fermi surface of the 4*f*-itinerant $CeIn_3$. Branches "*a*" and "*d*" are similar in shape between $LaIn_3$ (4*f*-localized $CeIn_3$) and the 4*f*-itinerant $CeIn_3$. Therefore, the volume of the main Fermi surface named "*a*" is very important to determine the character of the 4*f* electron in $CeIn_3$.

An important finding in the present pressure

experiment is that the drastic change of the dHvA frequency at $P_c \approx$ 2.60 GPa corresponds to the first-order phase transition. The similar instability of the Fermi surface is observed in $CeRh_2Si_2$ [3, 53] and $CeRhIn_5$ [54]. Moreover, the cyclotron mass m_c^* of the main Fermi surface named "*a*" is extremely large around : P_c: $m_c^* \approx$ 60 m_0 at 2.7 GPa for $H \parallel$ <1 0 0>, which is much larger than 0.46 m_0 in the corresponding Fermi surface in $ThIn_3$. The *d*-wave type superconductivity in $CeIn_3$ under pressure is closely related to this heavy fermion state around P_c.

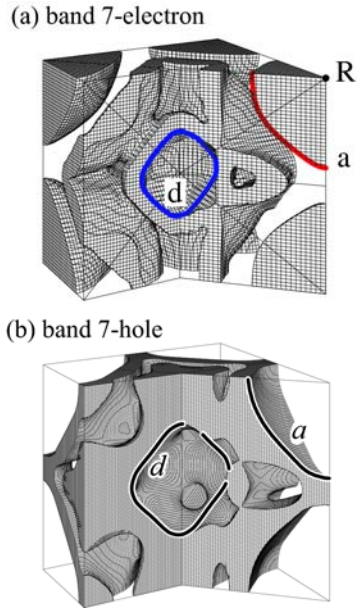

Fig. 23. Fermi surface of 4f-itinerant $CeIn_3$, presented by (a) the electron character and (b) the hole character.

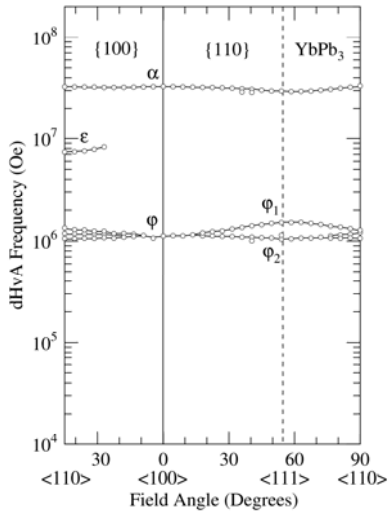

Fig. 24. Angular dependence of the dHvA frequency in a Pauli paramagnet $YbPb_3$.

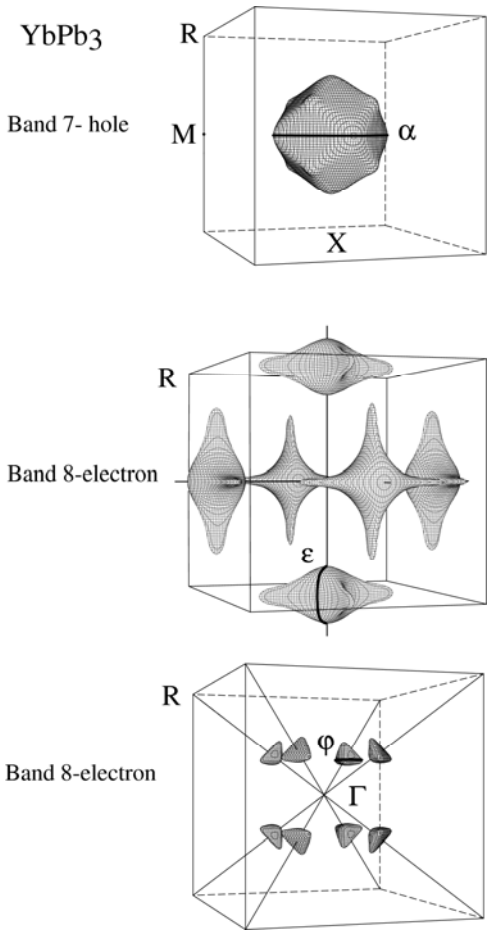

Fig. 25. Fermi surfaces in a Pauli paramagnet $YbPb_3$.

The next compound with the number of valence electrons, n = 14, corresponds to Pauli paramagnets $YbSn_3$ and $YbPb_3$ because Yb is divalent and the valence electrons in Sn and Yb are $5s^25p^2$ and $6s^26p^2$, respectively [55, 56]. Figure 24 indicates the angular dependence of the dHvA frequency in $YbPb_3$. The detected three branches named α, ε and φ are explained by the result of energy band calculation of which the Fermi surface is shown in Fig. 25. Here, the Fermi surface consists of a band 7-hole Fermi surface named α and band 8-electron Fermi surfaces named ε and φ, corresponding to a compensated metal as in $LaIn_3$ (n = 12).

Figure 26(a) shows the angular dependence of the dHvA frequency in $LaSn_3$ [57]. Main characteristic dHvA branches are as follows. Two branches named α and β exist in the whole range of angles, revealing two nearly spherical Fermi surfaces, three branches named γ_1, γ_2, and γ_3 are centered at <1 1 1>, and branch δ is centered at <1 1 0>.

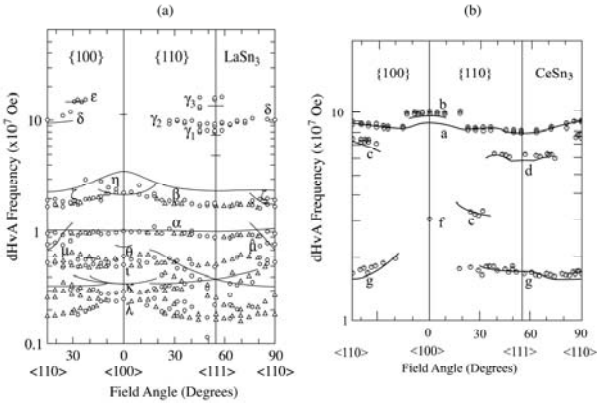

Fig. 26. Angular dependence of the dHvA frequency in (a) a non-4f reference compound $LaSn_3$ and (b) a 4f-itinerant $CeSn_3$. Solid lines are the results of energy band calculation.

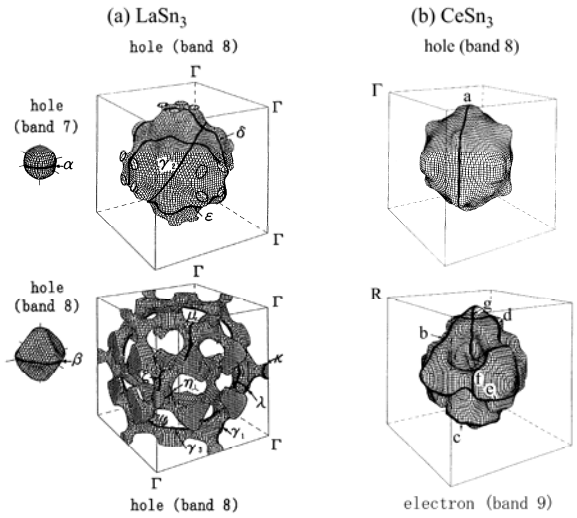

Fig. 27. Fermi surface of (a) $LaSn_3$ and (b) $CeSn_3$.

Compared with $LaIn_3$, $LaSn_3$ has three electrons more per primitive cell, and hence the electronic structure of $LaSn_3$ is that of an uncompensated metal. All the sheets of the Fermi surface in $LaIn_3$ disappear in $LaSn_3$. In $LaSn_3$, band 8 yields a main Fermi surface centered at R, and two small hole closed Fermi surfaces exist at Γ in bands 7 and 8, as shown in Fig. 27(a). The solid lines in Fig. 26(a) are the result of energy band calculation [58]. The detected dHvA branches are well explained on the basis of the Fermi surface in Fig. 27(a).

$CeSn_3$ at low temperatures is thought to belong to the so-called valence-fluctuation regime with a Kondo temperature of about 200 K. It is interesting to understand the 4*f*-electron character in comparison with the antiferromagnetic Kondo compound $CeIn_3$. Figure 26(b) shows the angular dependence of the dHvA frequency in $CeSn_3$ [59]. Some dHvA branches are similar but other branches are considerably different from those of $LaSn_3$. The detected cyclotron masses are roughly five times larger than those of $LaSn_3$: 4.2 m_0 for branch *a* in $CeSn_3$ and 0.91 m_0 for branch in $LaSn_3$, in agreement with γ values: 53 mJ/K^{2}mol in $CeSn_3$ and 11 mJ/K^{2}mol in $LaSn_3$.

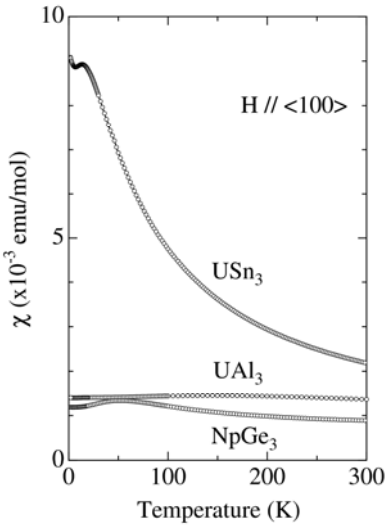

Fig. 28. Temperature dependence of the magnetic susceptibility in USn_3, UAl_3 and $NpGe_3$.

The energy band calculation was carried out under the assumption that the 4*f* electron is itinerant [60]. The calculated Fermi surfaces mainly consist of a large band 8 hole-Fermi surface centered at R and a large band 9 electron-Fermi surface centered at Γ. The origin of the analogy in Fermi surfaces between CeSn and LaSn3 is as follows. Namely, the large distorted spherical hole-Fermi surface of band 8 in $LaSn_3$ is similar to the band 8 hole-Fermi surface in $CeSn_3$. Small nearly spherical hole-Fermi surfaces in bands 7 and 8, denoted by α and β in $LaSn_3$, are also present in $CeSn_3$, not shown in Fig. 26(b) and Fig. 27(b), although their volumes of the Fermi surfaces in $CeSn_3$ are smaller than those of $LaSn_3$. The marked difference between $LaSn_3$ and $CeSn_3$ is ascribed to a large band 9 electron-Fermi surface in $CeSn_3$. Note that this Fermi surface has no occupied states along <1 1 1>.

The solid lines in Fig. 26(b) indicate the result of the 4*f*-itinerant energy band calculation. Branch *a* correspond to the large hole-Fermi surface, while the other main branches are due to the electron, indicating a compensated metal. Both in the magnitude of the cross-sectional area and in the observed range of angle, the 4*f*-itinerant band model agrees reasonably well with the experimental results. The reason for the disappearance of branch *a* at angles in the vicinity of the <1 0 0> direction is due to the combined effect of the curvature factor and cyclotron mass.

We will now turn to the compound with number of valence electrons, n=15, namely UAl_3, where the valence electrons are $5f^3 6d^1 7s^2$ in the U atom and $3s^2 3p^1$ in the Al atom. UAl_3 does not order magnetically, and the magnetic susceptibility possesses a broad maximum around

$T_{\chi\max} \cong 140$ K, as shown in Fig. 28. At higher temperatures up to 800 K, the susceptibility follows the Curie-Weiss law [61]. The effective magnetic moment μ_{eff}= 3.6 μ_B/U is close to 3.62 (3.58) μ_B /U in the 5*f*-localized $5f^3$($5f^2$) configuration. This is a reason why UAl_3 is characterized as a spin-fluctuating compound. The crossover from the 5*f*-localized electrons to the 5*f*-itinerant ones is supposed to occur below 140 K. It is thus important to clarify the 5*f*-electron character from the dHvA experiment and energy band calculation.

Figure 29 (a) and 29 (b) show the angular dependence of the dHvA frequency and the theoretical one based on the 5*f*-itinerant band model [62]. Among the detected several branches, two main branches named α and γ are well explained by the theoretical closed band 8-hole Fermi surfaces, as shown in Fig. 30.

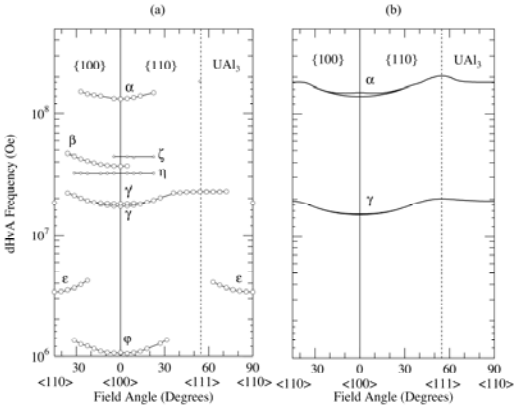

Fig. 29. (a) Angular dependence of the dHvA frequency in a heavy-fermion compound UAl_3 and (b) the theoretical one.

One large Fermi surface is nearly cubic, centered at Γ, and the other small Fermi surface is also nearly cubic, centered at R. The detected cyclotron mass is in the range from 3 to 17 m_0 , suggesting the strong 5f hybridization with the conduction electrons, which is twice to three times larger than the corresponding band mass: m_c^*=17 m_0 and m_b=6 m_0 for branch α, and γ = 47 mJ/K^{2}mol and γ_β= 14.8 mJ/K^{2}mol.

UGa_3 and Uin_3 are the compounds with n = 15, similar to UAl_3. Both compounds, however, order antiferromagnetically below T_N= 67 K and 90 K, respectively. UGa_3 was studied on the basis of the 5*f*-itinerant antiferromagnet [63], but the detected dHvA branches in UGa_3 are not explained by the spin-polarized 5*f*-itinerant band model, which is most likely due to the magnetic structure, not definitely determined yet. Here we show in Figs. 31 and 32 the angular dependence of the dHvA frequency in UGa_3 [64] and Uin_3 [65], respectively.

The compound with the number of electrons, n = 17, corresponds to $PuIn_3$, as shown in Table 5. It is, however, better to present the corresponding Fermi surface property as a final compound in RX_3 and AnX_3. We will go on to USi_3 with n = 18. USi_3 is a Pauli paramagnet with a small γ value of 11.9 mJ/K^{2}mol. Figures 33(a) and 33(b) show the angular dependence of the dHvA frequency and the corresponding theoretical one based on the 5*f*-itinerant band model, respectively [66]. Fifteen dHvA branches are observed, ranging from 7.37×10^6 to 2.33×10^8 Oe, which are in good agreement with the theoretical ones based on the 5*f*-itinerant Fermi surfaces shown in Fig. 34. Theoretically, the 5*f* electrons form wide bands across the Fermi energy, which hybridize considerably with Si-3*p* electrons. The *p*-*f* hybridization makes the dispersion of the 5*f*-bands very large. Cyclotron masses, which are in the range from 0.39 to 4.17 m_0 , are thus approximately the same as the corresponding band masses, being in good agreement with a relation between the γ value of 11.9 mJ/K^{2}mol and γ_b = 11.7 mJ/K^{2}mol. The mass enhancement is thus extremely small in USi_3.

A small mass enhancement is observed in UGe_3 with γ = 20 mJ/K^{2}mol, with the same topology of the Fermi surface as in USi_3, from the dHvA experiment and energy band calculation [67], while a relatively large mass enhancement is expected in a spin-fluctuating compound USn_3 with γ = 170 mJ/K^{2}mol, as shown in Fig. 1(b). As noted in Chap. 3, the metamagnetic transition is observed at H_m = 310 kOe in the magnetization curve, as shown in Fig. 7. Figure 35 shows the angular dependence of the dHvA frequency in USn_3. Only branches μ_i are observed. The cyclotron mass of branches $\mu_{2,3}$ for H || <1 0 0> is 1.5 m_0 in USn_3, which is large compared with m_0 0.40 in USi_3 and m_0 0.42 in UGe_3.

The next compound is $NpGe_3$ with n = 19. This is an enhanced Pauli paramagnet, similar to UAl_3. The magnetic susceptibility has a maximum around 50 K, as shown in Fig. 28. From the susceptibility data above 250 K, the estimated effective magnetic moment is μ_{eff} = 2.78 μ_B/Np, which is close to μ_{eff}= 2.68μ_B /Np in Np^{3+} ($5f^4$), but is smaller than μ_{eff} = 3.62μ_B /Np in Np^{3+} ($5f^3$). The present result of the magnetic susceptibility suggests that the Np ion possesses a local moment at high temperatures, but the electronic state is changed into the enhanced Pauli paramagnet at temperatures lower than 50 K.

Fig. 36(a) and (b) show the angular dependence of the dHvA frequency and the corresponding one based on the 5*f*-itinerant Fermi surfaces shown in Fig. 37, being in good agreement between experiment and theory [68]. The band 10 electron-Fermi surface in USi_3 (UGe_3), shown in Fig. 34(c), is spherical, but possesses a hollow space at the center and a window for <1 0 0>, with a flat closed Fermi surface at the M point. One more 5*f* electron becomes a valence electron in $NpGe_3$. This means that the hole bands (8 and 9) are occupied completely by the electron and also the band 10 electron-Fermi surface, centered at R, is partially occupied by the remaining electron, producing a hollow ball with a "belly" orbit and a "neck". The cyclotron mass is in the range of 2.6 to 16 m_0, which is enhanced approximately 3.5 times from the corresponding band mass. This is in fairly good agreement with the ratio of γ = 34 mJ/K^{2}mol to γ_b = 16.8 mJ/K^{2}mol, γ/γ_b = 2.0. It is noted that the cyclotron mass and the corresponding band

mass for an outer "belly" orbit δ_2 are m_c^* =4.7 m_0 and m_b=1.35 m_0 , respectively, which are compared with m_c^*=15 m_0 and m_b=4.03 m_0 for an inner orbit β. This is because the inner part of the band 10 electron-Fermi surface is mainly due to the contribution of 5*f* electrons of Np, while the outer part is due to the 4*p* component of Ge.

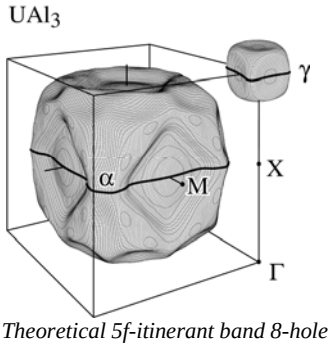

Fig. 30. Theoretical 5f-itinerant band 8-hole Fermi surfaces in UAl_3.

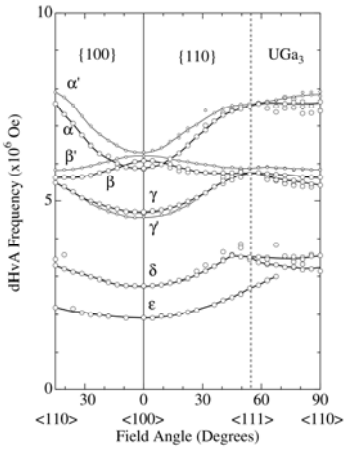

Fig. 31. Angular dependence of the dHvA frequency in an antiferromagnet UGa_3.

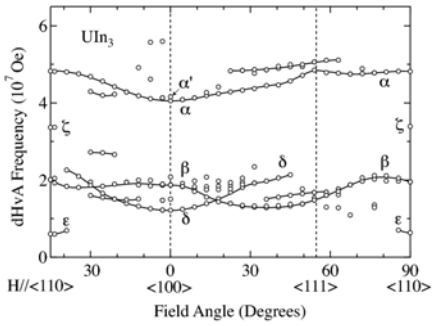

Fig. 32. Angular dependence of the dHvA frequency in an antiferromagnet UIn_3.

Next we would like to discuss the electronic state of a complicated magnetic compound $NpIn_3$ [69]. Ferromagnetic and antiferromagnetic orderings occur at T_C=14 K and T_N=10 K, respectively, together with another transition at T^*=8 K. When the magnetic field is applied to the sample, the antiferromagnetic state is finally changed into a ferromagnetic state with two metamagnetic transitions at H_{c1} and H_{c2}. The antiferromagnetic ordering and two metamagnetic transitions are found to be of the first-order phase transition. We show in Fig. 38 the magnetic phase diagram for three principal directions [69]. All the dHvA signals are detected in the ferromagnetic state, namely above H_{c2}.

Figure 39 shows the angular dependence of the dHvA frequency. Since the ferromagnetic state is not realized at the highest magnetic field of 150 kOe for the magnetic field around the <1 0 0> direction, as shown in Fig. 38, no dHvA signals are observed around <1 0 0>. Three dHvA branches named α, β and γ are observed. Branches α and β correspond to nearly spherical Fermi surfaces. The dHvA frequency of branch γ increases with increasing the field angle from <1 0 0> to <1 1 0> or <1 1 1>. At 31^0 (to <1 1 0> and 36^0 (to <1 1 1>), branch γ abruptly disappears, suggesting the open orbit, which is most likely due to a multiply-connected Fermi surface.

From the present dHvA results, we constructed the Fermi surface of $NpIn_3$. Two cases can be considered. The one is the case based on the 5*f*-itinerant picture. Another is the case based on the 5*f*-localized picture. In the case of 5*f*-itinerant picture, the total number of valence electrons in $NpIn_3$ is even, namely 16, where the electronic configurations are Np ($5f^46d^17s^2$) and In ($5s^25p^1$). This means that $NpIn_3$ is a compensated metal with equal carrier numbers of electrons and holes.

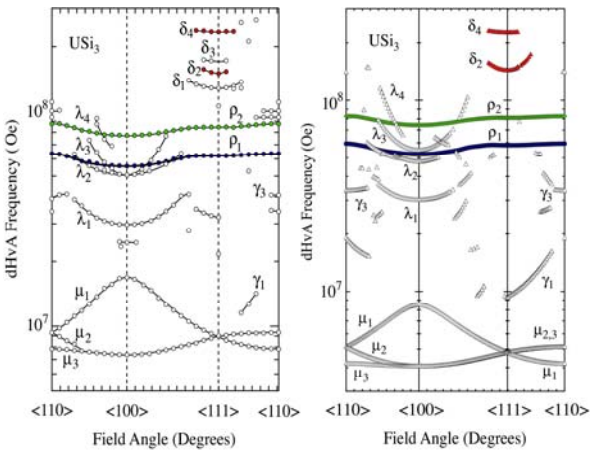

Fig. 33. (a) Angular dependence of the dHvA frequency in a Pauli paramagnet USi_3 and (b) the theoretical one.

In the case of a 5*f*-localized picture, the Np^{3+} (5) configuration might be applicable to $NpIn_3$, because the magnetic effective moment is close to the value for the Np^{3+} free ion. Moreover, the Mössbauer measurement indicates the Np^{3+} valence state from the isomer shift [70]. In this case, the total number of valence electrons is 12, which is also even in number, meaning that $NpIn_3$ is a compensated metal.

Both 5*f*-itinerant and localized pictures deduce $NpIn_3$ as a compensated metal. Thus we restrict ourselves to a compensated metal of $NpIn_3$ in order to construct the Fermi surface from the present dHvA results on the basis of the 5*f*-localized Np^{3+} ($5f^4$) configuration. We note that

the Brillouin zone in the ferromagnetic state is the same as that in the paramagnetic state. Thus it is possible to treat NpIn as a compensated metal in the same way as in the paramagnetic state.

On the basis of the 5*f*-localized Np^{3+} ($5f^4$) configuration and the Fermi surface of $LaIn_3$, we constructed the Fermi surface in the ferromagnetic state of $NpIn_3$, as shown in Fig. 40. Characteristic features of the Fermi surface properties in $NpIn_3$ are as follows. A spherical Fermi surface with a relatively small cyclotron mass of $4m_0$ in $NpIn_3$ corresponds to a spherical electron Fermi surface in $LaIn_3$. A complicated hole-Fermi surface in LaIn is simply modified to a multiply-connected Fermi surface with arms along <1 0 0> and vacant space at the center in $NpIn_3$, whose cyclotron masses are large: about $6m_0$ for the arm and 12-14m_0 for a spherical Fermi surface (vacant space).

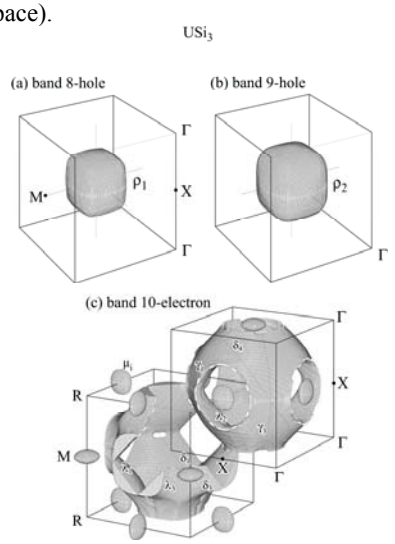

Fig. 34. Theoretical 5f-itinerant Fermi surfaces in USi_3.

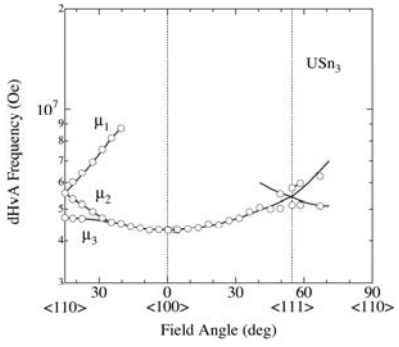

Fig. 35. Angular dependence of the dHvA frequency in a spin-fluctuation compound USn_3.

Finally we present the dHvA experiment for $PuIn_3$ with n = 17, where the valence electrons are $5f^5 6d^1 7s^2$ in the Pu atom and $5s^2 5p^1$ in the In atom [71]. As noted above, the Wigner-Seitz radius of Pu is an intermediate value between Np with the 5*f*-itinerant nature and Am with the 5*f*-localized nature. It is thus a challenging study to clarify the electronic state of Pu compounds. The recent discovery of superconductivity in $PuCoGa_5$ and $PuRhGa_5$ with a superconducting transition temperature T_{sc}= 18.5 and 9 K, respectively, as described later, has accelerated the studies of the electronic states in the Pu compounds. Here we show the first dHvA effect in $PuIn_3$.

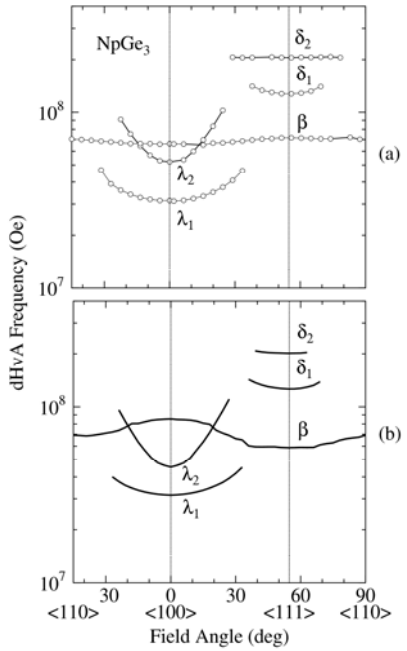

Fig. 36. (a) Angular dependence of the dHvA frequency in a heavy-fermion compound $NpGe_3$ and (b) the theoretical one.

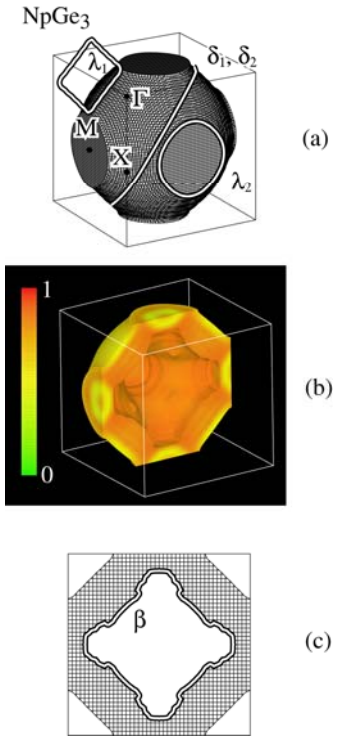

Fig. 37. Theoretical 5f-itinerant Fermi surfaces and cross-sections in $NpGe_3$. The color presents the contribution of 5f-electrons.

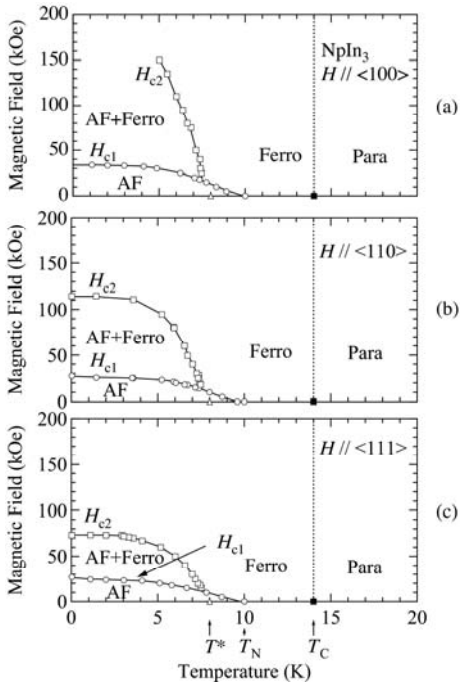

Fig. 38. Magnetic phase diagram in an antiferromagnet $NpIn_3$.

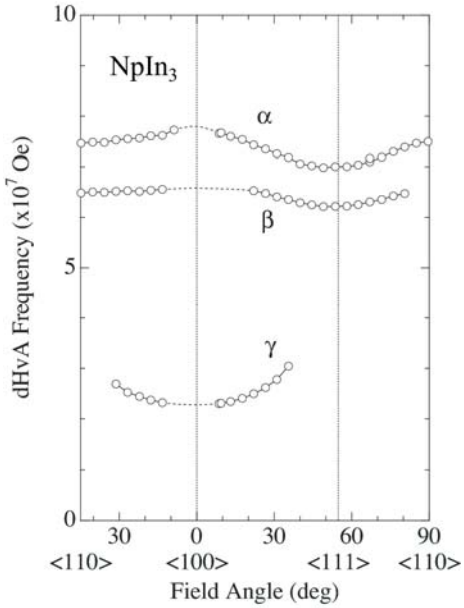

Fig. 39. Angular dependence of the dHvA frequency in an antiferromagnet $NpIn_3$.

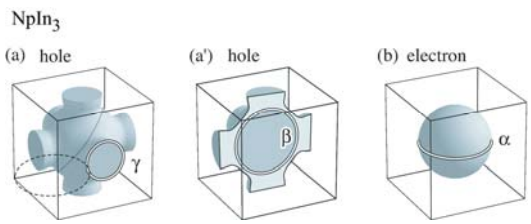

Fig. 40. Proposed Fermi surfaces in the field-induced ferromagnetic state of $NpIn_3$.

Fig. 41 shows the dHvA oscillations and their FFT spectra [71]. It is noted that the dHvA amplitude of branch γ in EX 1 is extremely reduced at EX 2, where the dHvA experiment named EX 2 was done one week later than the first experiment named EX 1. An intensive reduction of the dHvA amplitude is due to point defects produced by α-decay of Pu. On the other hand, the dHvA amplitude of $F = 5.5 \times 10$ Oe is the same between EX 1 and EX 2, which is not due to branch in PuIn but due to a dHvA signal of impurities, most likely In. Figure 42 shows the angular dependence of the dHvA frequency, where branch γ is observed around <1 1 1>. Solid lines in Fig. 42 are the result of 5*f*-itinerant band calculation. Branch γ corresponds to a small spherical electron Fermi

Fermi surface centered at the Γ point, where two kinds of spherical Fermi surface are theoretically obtained on the basis of the 5*f*-itinerant band model, as shown in Fig. 43. The cyclotron mass of branch γ is 4.8 m_0, which is three times larger than the corresponding band mass of 1.56 m_0. A relatively large cyclotron mass of 17 m_0 might be expected for branch α along $H\|$ <1 1 0>. On the basis of the results of energy band calculation, the contribution of the 5*f* component to Fermi surfaces is approximately 50% for branches α and γ, while it is 70% for branch β. It is noticed that these Fermi surfaces in $PuIn_3$ are approximately the same as those of $YbIn_3$ with $n = 11$ in topology, as shown in Figs. 10 and 11, although there exists no contribution of 4*f* electrons to the Fermi surfaces in $YbIn_3$.

The Fermi surface properties such as 5*f*-itinerant characteristics and the enhanced cyclotron mass in $PuIn_3$ are very similar to those in the enhanced paramagnet $NpGe_3$, mentioned above. $PuIn_3$ is most likely an enhanced paramagnet, although the fundamental properties such as the magnetic susceptibility and specific heat are needed to be clarified in $PuIn_3$.

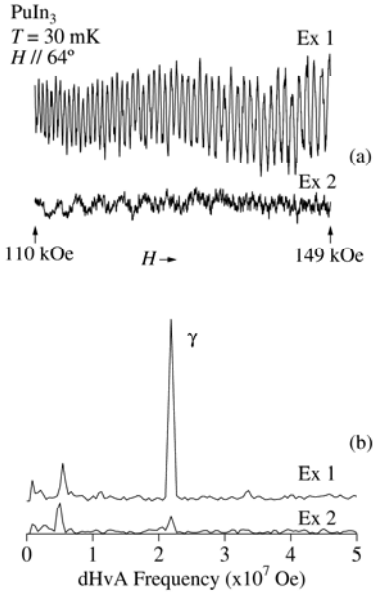

Fig. 41. (a) dHvA oscillations and (b) the corresponding FFT spectra in a paramagnet $PuIn_3$.

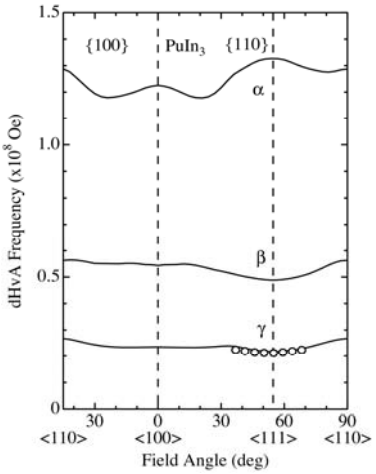

Fig. 42. Angular dependence of the dHvA frequency in a paramagnet $PuIn_3$. Solid lines are the results of 5f-itinerant energy band calculation.

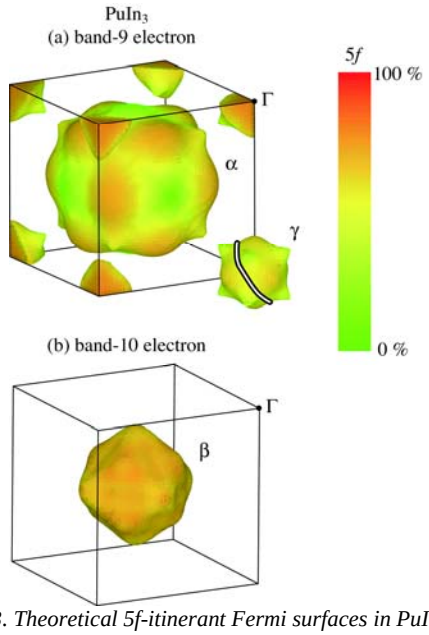

Fig. 43. Theoretical 5f-itinerant Fermi surfaces in $PuIn_3$. The color presents the contribution of 5f-electrons.

Table 6. Number of valence electrons and Fermi surface studies in RTX_5 and $AnTX_5$ compounds with the $HoCoGa_5$-type tetragonal structure.

number of valence electrons	compounds	refs.
27	$LaRhIn_5$ $CeRhIn_5$ (AF)	[75]
28	$CeRhIn_5$ under pressure	[54]
	$CeCoIn_5$ $ThRhIn_5$	[31] [79]
29	$UFeGa_5$	[85]
30	$UCoGa_5$	[86]
31 (63)	$UPtGa_5$ (AF) $NpRhGa_5$ (AF)	[88] [89]
32	$PuCoGa_5$ $PuRhGa_5$	[95] [96]

5. Fermi surface properties in RTX_5 and $AnTX_5$

Next we present the Fermi surface properties of RTX_5 and $AnTX_5$ with the $HoCoGa_5$-type tetragonal structure, as shown in Fig. 8(b). RTX_5 and $AnTX_5$ are classified according to the number of valence electrons, as shown in Table 6.

We show in Fig. 44 the electronic states in $CeTIn_5$, $ThTIn_5$ and $AnTGa_5$, indicating paramagnetism, antiferromagnetism (AF), ferromagnetism (F) and superconductivity (SC) [72-74]. The crystal structure in Fig. 8(b) is characteristic, which is closely related to the electronic state. Namely, the uniaxially distorted $AuCu_3$-type layers of RX_3 (AnX_3) and the TX_2 layers are stacked sequentially along the [0 0 1] direction (*c*-axis). For example, the 4*d* electrons of Rh in $LaRhIn_5$ hybridize with the 5*p* electrons of In, which results in a small density of states around the Fermi energy. This means that there are very few conduction electrons in the $RhIn_2$ layer and hence the $LaIn_3$ layer is conductive, producing cylindrical Fermi surfaces. This is also applicable to all the RTX_5 and $AnTX_5$ compounds, except $UTGa_5$ (T: Co, Rh and Ir), shown later.

Figures 45(a) and (b) show the angular dependence of the dHvA frequency and the theoretical one in $LaRhIn_5$ [75]. Main detected dHvA branches named (i = 1, 2 and 3) and (i = 1 and 2) are the same as the theoretical ones. These dHvA branches are well identified by the theoretical Fermi surfaces in Fig. 46. The dHvA branches are due to a band 15-electron Fermi surface, which is nearly cylindrical but highly corrugated, having maximum and minimum cross-sections. Branches β_i are also due to a highly-corrugated band 14-electron Fermi surface. This Fermi surface has a convex part stretching along the [1 1 0] direction. This is the main reason why the dHvA frequency of branch has a minimum at about 30°.

Here, the electronic configuration in $LaRhIn_5$ is [Xe] $5d^16s^2$ in the La atom, [Kr] $4d^85s^1$ in the Rh atom and [Kr] $5s^25p^1$in the In atom. The valence electrons are 27 in number, as shown in Table 6, indicating an uncompensated metal for $LaRhIn_5$. In an antiferromagnet $CeRhIn_5$, the 4*f* electrons are considered to be localized at the Ce sites with magnetic moments of $0.8\mu_B$ /Ce [72], where the electronic configuration of the Ce atom is [Xe] $4f^15d^16s^2$. The detected main dHvA branches in $CeRhIn_5$ are thus approximately the same as those of $LaRhIn_5$ [75].

With increasing pressure P for $CeRhIn_5$, the Néel temperature = 3.8 K increases, has a maximum around 1 GPa, and decrease with increasing pressure. A smooth extrapolation indicates that $T_N \rightarrow 0$ at P_c = 2.3 - 2.5 GPa, as shown in Fig. 47. Figure 48 (a) and 48 (b) show the temperature dependence of the electrical resistivity in $CeRhIn_5$ under pressure. At 1.60 and 1.89 GPa, superconductivity, as well as antiferromagnetic ordering, shown by arrows, are clearly observed. Only superconductivity is observed at 2.08 GPa. Around the critical pressure region, $CeRhIn_5$ reveals superconductivity, with a maximum transition temperature T_{sc}= 2.2 K [76]. From the NQR and specific heat experiments, together with the dHvA experiment shown below, the critical pressure is P_c (H=0) ≈ 2.0 GPa at zero field [77], whereas ($H \neq 0$) ≈ 2.3 GPa in magnetic fields

[78, 54].

Fig. 49 shows the pressure dependence of the dHvA frequency and the cyclotron effective mass m_c^* in $CeRhIn_5$. A marked change of the dHvA frequencies occurs above $P_c \approx 2.35$ GPa [54]. The detected dHvA frequencies above $P_c \approx 2.35$ GPa are consistent with those of a non-magnetic heavy-fermion superconductor $CeCoIn_5$ of which the dHvA branches are well explained by the 4*f*-itinerant band model [31]. A change of the 4*f*-electron nature from localized to itinerant is realized at $P_c \approx 2.35$ GPa, revealing the first-order phase transition, together with a divergent tendency of the cyclotron effective mass m_c^* at P_c. The appearance of superconductivity in $CeRhIn_5$ is closely related to the present heavy-fermion state.

Here, the number of valence electrons in $CeCoIn_5$ is 28, as shown in Table 6, because the 4*f* electron in the Ce atom becomes itinerant at low temperatures, as noted above. $CeCoIn_5$ thus becomes a compensated metal. Namely, the volume of the electron Fermi surface is equal to that of the hole Fermi surface. The same number of valence electrons is realized in a Pauli paramagnet $ThRhIn_5$, where the electronic configuration is $[Rn]6d^27s^2$ in the Th atom.

We show in Fig. 50 the angular dependence of the dHvA frequency in $CeCoIn_5$ and $ThRhIn_5$. The detected dHvA branches named α_i and β_2 in $ThRhIn_5$ are approximately the same as those of $CeCoIn_5$ [79]. The cyclotron mass is, however, highly different between them. The cyclotron mass in CeCoIn at low fields is estimated as $100m_0$ in branch β_2 and 30 m_0 in branches α_i, as shown in Fig. 51. The large cyclotron mass in $CeCoIn_5$ is field-dependent, and decreases as a function of the magnetic field. This is characteristic in heavy fermions. These cyclotron masses are large compared with 0.87 m_0 in branch β_2 and 0.89 - 0.95 m_0 in branches α_i in $ThRhIn_5$. The large cyclotron mass in $CeCoIn_5$ is mainly due to the many-body Kondo effect. It is clarified from the energy band calculation that the 4*f*-electron contribution to the density of states at the Fermi energy is about 70 % in magnitude.

The characteristic features of superconductivity in $CeCoIn_5$ are as follows. Superconductivity is of the $d_{x^2-y^2}$ type, with line nodes along the [0 0 1] direction on the quasi-two dimensional Fermi surfaces, which was clarified from the angular dependence of the thermal conductivity in magnetic fields [80]. We show schematically the gap with the line nodes in Fig. 52. The first-order phase transition from the superconducting mixed state to the normal state occurs at H_{c2} [81], as shown later in Fig. 69(b). The Fulde, Ferrel, Larkin, Ovchinikov (FFLO) state most likely exists in the superconducting mixed state close to H_{c2} at temperatures far lower than $T_{sc} = 2.3$ K [82, 83]. These are closely related to the strong Pauli paramagnetic effect in the present superconductivity of $CeCoIn_5$.

$CeTIn_5$	$ThTIn_5$	$UTGa_5$			$NpTGa_5$			$PuTGa_5$
Co SC 2.3 K		Fe	Co	Ni AF 86 K [b] (0.75 μ_B)	Fe AF 118 K [b] (0.86 μ_B)	Co AF 47 K [b] (0.8 μ_B)	Ni AF,F 30 K [c] (0.8 μ_B)	Co SC 18.5 K
Rh AF 3.8 K [a] (0.8 μ_B)	Rh	Ru	Rh	Pd AF 30 K [b] (0.33 μ_B)		Rh AF 36 K [b] (0.96 μ_B)		Rh SC 9 K
Ir SC 0.4 K		Os	Ir	Pt AF 26 K [b] (0.32 μ_B)			Pt AF 26 K [b] (0.5 μ_B)	

Fig. 44. Electronic states in $CeTIn_5$, $ThRhIn_5$ and $AnTGa_5$, where AF, F, and SC correspond to antiferromagnetism, ferromagnetism and superconductivity, respectively. The transition temperature (the magnitude of the magnetic moment in the ground state) are shown. The magnitudes of magnetic moments indicated by a, b and c are cited from refs. [72] [73] [74], respectively.

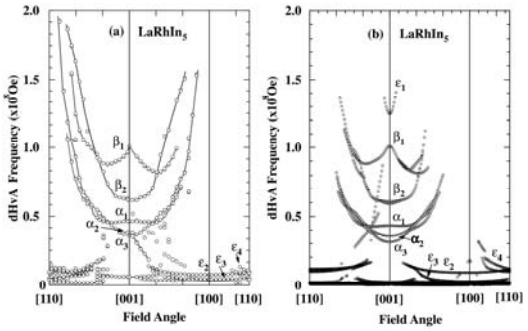

Fig. 45. Angular dependence of (a) the dHvA frequency and (b) the theoretical one in a non-4f reference compound $LaRhIn_5$.

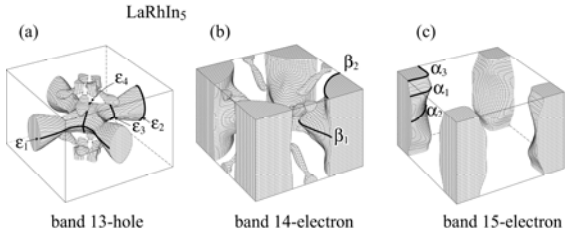

Fig. 46. Theoretical Fermi surfaces of $LaRhIn_5$.

We show in Fig. 53(a) the temperature dependence of the magnetic susceptibility. The susceptibility increases steeply with decreasing temperature, but a sudden drop of the susceptibility occurs below $T_{sc} = 2.3$ K due to the onset of superconductivity. This is not usual. In the case of a typical heavy fermion superconductor UPt_3, the magnetic susceptibility has a maximum at $T_{\chi max} \approx 20$ K, and becomes constant at temperatures lower than $T_{\chi max}$, as shown in Fig. 2. Superconductivity occurs below $T_{sc} = 0.5$ K. This means that superconductivity is realized after the heavy fermion state is completely formed. On the other hand, the heavy fermion state is not completely formed at $T_{sc} = 2.3$ K in $CeCoIn_5$.

This can be seen in the specific heat data. Figure 54 shows the temperature dependence of the specific heat in the form of C/T under magnetic fields. The value of C/T increases with decreasing temperature under magnetic fields. The γ value is 380 mJ/K^2mol at $T_{sc} = 2.3$ K, but is

extremely enhanced to be 1070 mJ/K^{2}mol at 0.2 K. Note that the upper critical field H_{c2}= 49.5 kOe for H|| [0 0 1]. The specific heat in the form of C/T in the normal state (under H = 60 kOe) does not saturate at low temperatures, but increases with decreasing temperature. The nature of the non-Fermi liquid state is thus observed in the specific heat, together with the magnetic susceptibility. This is also observed in the electrical resistivity. The electrical resistivity follows a T-linear dependence below 10 K, as shown in Fig. 48(d). Moreover, the upper critical field H_{c2} (0) and cyclotron mass m_c^* decrease monotonically with increasing pressure [84]. These results indicate that the electronic state of $CeCoIn_5$ is very close to the quantum critical point at ambient pressure.

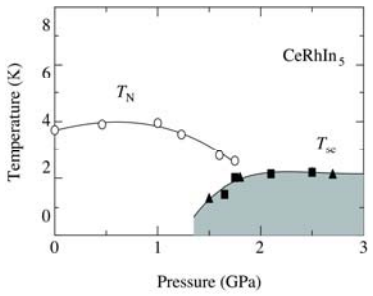

Fig. 47. Pressure phase diagram in an antiferromagnet $CeRhIn_5$.

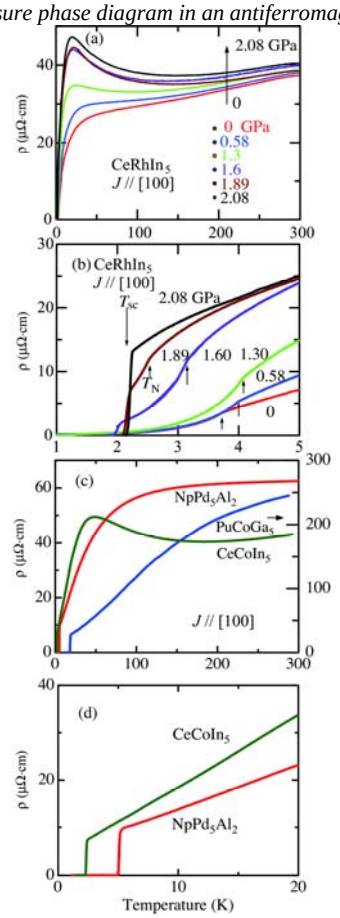

Fig. 48. Temperature dependence of the electrical resistivity in (a) and (b) $CeRhIn_5$ under pressure, and (c) and (d) $CeCoIn_5$, $PuCoGa_5$ and $NpPd_5Al_2$. Only $PuCoGa_5$ is a polycrystal sample, and the scale is shown by the right hand in (c), cited from ref. [93].

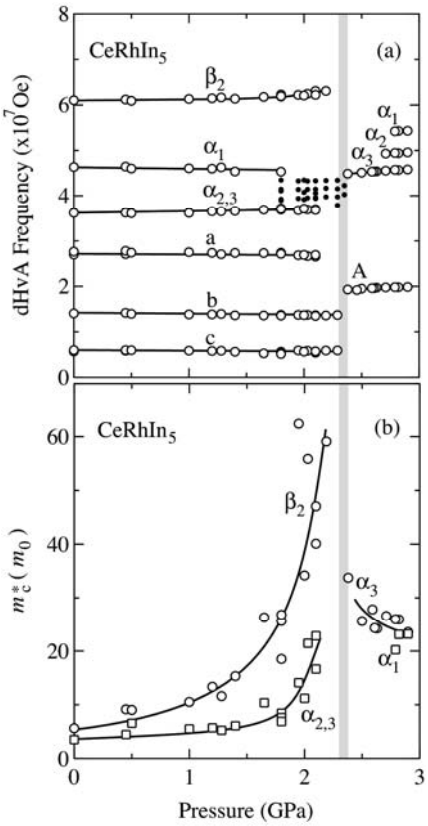

Fig. 49. Pressure dependence of (a) the dHvA frequency and (b) the cyclotron mass in an antiferromagnet $CeRhIn_5$.

The next compound is a Pauli paramagnet $UFeGa_5$ with the number of valence electrons, 29, as shown in Table 6, where the electronic configuration is [Rn]5f^{3}6d^{1}7s^2 in the U atom and [Ar]3d^{6}4s^2 in the Fe atom. Here we briefly note the electronic states in $UTGa_5$. Figure 55 shows the temperature dependence of the magnetic susceptibility. $UTGa_5$ (T: Fe, Ru, Os, Co, Rh, Ir) compounds are Pauli paramagnets, while $UTGa_5$ (T: Ni, Pd, Pt) order antiferromagnetically.

We show in Fig. 56 the angular dependence of the dHvA frequency and the corresponding theoretical one for $UFeGa_5$ [85]. The detected dHvA branches are consistent with the theoretical ones based on the 5*f*-itinerant band 15 electron-Fermi surfaces shown in Fig. 57. The Fermi surface consists of a corrugated but cylindrical Fermi surface and a lattice-like Fermi surface. The cyclotron mass is relatively large, ranging from 2.4 to 9.9 m_0: 9.2 m_0 for branch α_i and 9.9 m_0 for branch *a*. The theoretical band mass is about half of the experimental one, which is consistent with a relation between γ = 40 mJ/K^{2}mol and the theoretical one γ_b= 19.6 mJ/K^{2}mol.

In a Pauli paramagnet $UCoGa_5$ with the number of valence electrons, n = 30, as shown in Table 6, we observed dHvA branches with small dHvA frequencies, indicating a semimetal [86]. We show in Fig. 58 the angular dependence of the dHvA frequency. Three kinds of dHvA branches named *a*, *b* and *c* correspond to small ellipsoidal Fermi surfaces. We constructed the Fermi

surfaces by using the present dHvA data so as to become the semimetal with equal volumes of electron and hole Fermi surfaces, as shown in Fig. 59. The Fermi surface consists of small band 15-hole Fermi surfaces (branches *b* and *c*) and a small band 16-electron Fermi surface (branch *a*) because one more valence electron is added, compared with that in $UFeGa_5$, and the number of valence electrons is 30 in $UCoGa_5$, revealing a compensated metal or a semimetal. The γ value of $UCoGa_5$ is small, γ = 3.3 mJ/Kmol, which corresponds to a light cyclotron mass of m_c^* = 0.82 in branch *a* for *H*|| [0 0 1].

The next compound is $UPtGa_5$ with the number of valence electrons, n = 31, as shown in Table 6. $UPtGa_5$ is, however, an antiferromagnet with the Néel temperature T_N = 26 K and a small ordered moment μ_s= 0.32μ_B /U, as shown in Fig. 60 [87]. $UPtGa_5$ is supposed to be a 5*f*-itinerant antiferromagnet, similar to UGa_3. It is however, noticed that the magnetic susceptibility follows the Curie-Weiss law above 500 K, with effective magnetic moments of 3.5 and 3.2μ_B /U for *H*|| [0 0 1] and [1 0 0], respectively, as shown in Fig. 61 [61]. These effective moments are close to the free ion value of μ_{eff} = 3.58 μ_B /U for $5f^3$ (U^{3+}) or = 3.62μ_B /U for $5f^2$ (U^{4+}), as shown by a solid line in Fig. 61, indicating the localized nature of 5*f* electrons at high temperatures.

A ferromagnetic coupling in the basal (0 0 1) plane was observed by the neutron scattering experiment, which is stacked along the [0 0 1] direction with an antiferromagnetic (↑ ↓) sequence, as shown in Fig. 60 . Therefore, the magnetic unit cell becomes doubled, containing the 62 valence electrons. In other words, the magnetic Brillouin zone becomes flat along the [0 0 1] direction.

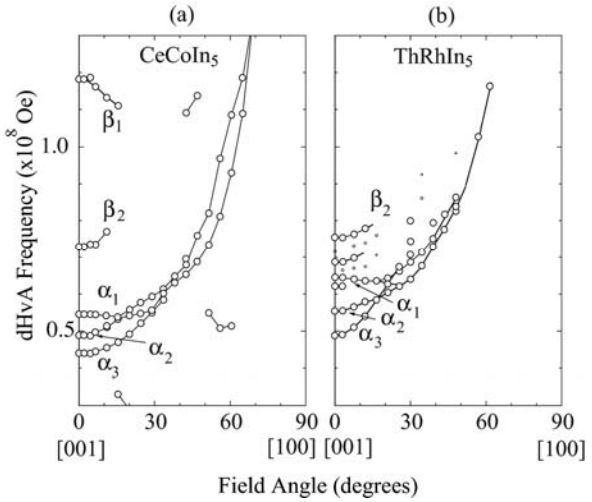

Fig. 50. Angular dependence of the dHvA frequency of (a) a non-magnetic heavy-fermion superconductor $CeCoIn_5$ and (b) a Pauli paramagnet $ThRhIn_5$.

We show in Fig. 62 the angular dependence of the dHvA frequency in the antiferromagnetic state. The detected dHvA branches named α_1, α_2, α_3 and γ and ε roughly follow the 1/cosθ dependence (θ: the tilted angle from [0 0 1] to [1 0 0] or [1 1 0]), revealing cylindrical Fermi surfaces. These branches are well explained by the spin (orbital)-polarized 5*f*-itinerant band model, as shown in Fig. 62(b) [88]. The Fermi surface shown in Fig. 63 consists of four kinds of corrugated but cylindrical Fermi surfaces. Branches ε, α_3, α_1 , α_2 and γ correspond to orbit *a* of the band 31-hole Fermi surface, orbits d_1 and d_2(band 32-electron), orbits e_1 and e_2 (band 33-electron) and orbits and (band 30-hole), respectively. The cyclotron effective masses are relatively large: 20 m_0 (branch ε), 24 m_0 (branch), 13 and 10 m_0 (branches , , respectively) and 10 m_0 (branch γ). These values are consistent with γ = 57 mJ/K^{2}mol. It is stressed here that the almost localized nature of the 5*f* electrons at high temperatures is changed into the 5*f*-itinerant character, with a small ordered moment of 0.32μ_B /U.

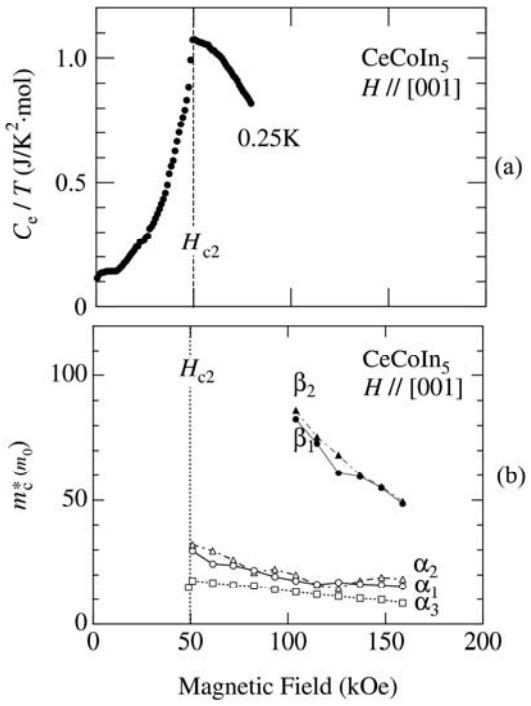

Fig. 51. Field dependence of the cyclotron mass in $CeCoIn_5$.

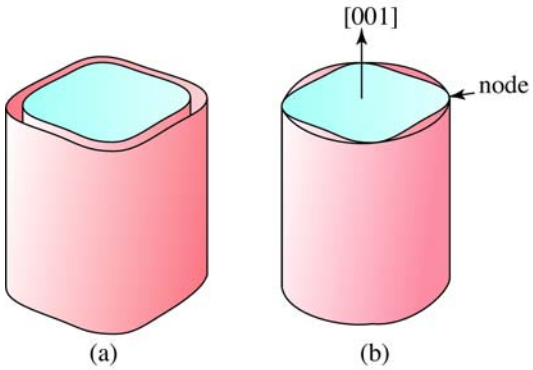

Fig. 52. Schematic pictures of the two dimensional superconducting gap with (a) an isotropic gap and (b) a line node gap.

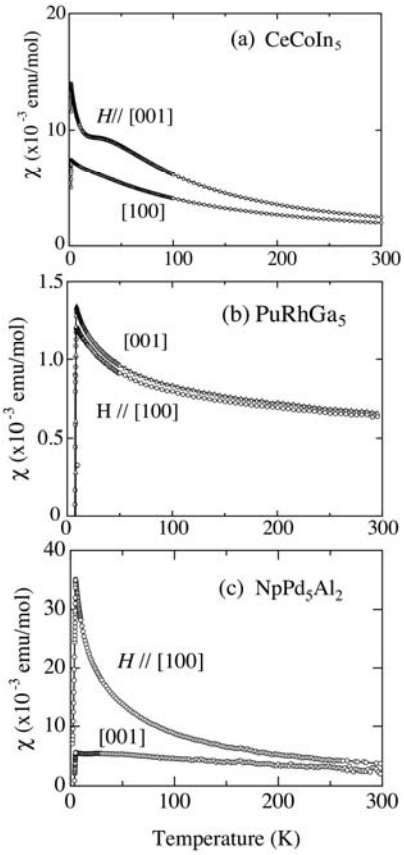

Fig. 53. Temperature dependence of the magnetic susceptibility in (a) $CeCoIn_5$, (b) $PuRhGa_5$ and (c) $NpPd_5Al_2$.

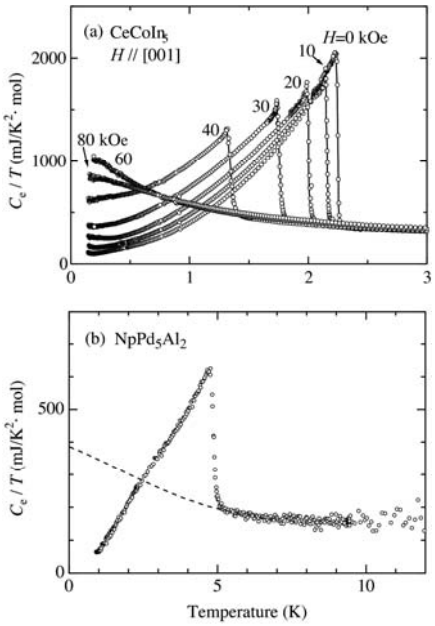

Fig. 54. Temperature dependence of the electronic specific heat in the form of in (a) $CeCoIn_5$ and (b) $NpPd_5Al_2$.

The similar magnetic structure is realized in an antiferromagnet $NpRhGa_5$, and the corresponding angular dependence of the dHvA frequency is similar to that of $UPtGa_5$, as shown in Fig. 64 [89]. The magnetic property of $NpRhGa_5$ is very interesting. There are two successive antiferromagnetic transitions at T_{N1} = 36 K and T_{N2} = 32 K. The magnetic structure in the temperature range from T_{N1} to T_{N2} is the same as that in $UPtGa_5$ [90]. We show in Fig. 65 the magnetic phase diagram for $H\|$ [0 0 1] [91]. Below , the direction of the magnetic moment changes abruptly from [0 0 1] to [1 1 0]. The ordered moment is most likely enhanced from $0.6\mu_B$ /Np to $0.96\mu_B$ /Np. The former value is an ordered moment, estimated under the assumption that the AF1 phase persists down to 0 K without the magnetic transition at T_{N2}. The latter value of $0.96\mu_B$ /Np is determined experimentally at low temperatures far below T_{N2} . It is theoretically pointed out that the quadrupolar interaction plays an important role on this transition at T_{N2} [92].

Here we note that $NpTGa_5$ order antiferromagnetically, which are in contrast with the electronic states in $UTGa_5$, indicating paramagnetism and antiferromagnetism, as shown in Fig. 44. Moreover, the ordered moments in neptunium compounds are roughly twice larger than those in uranium compounds. This is the reason why the magnetic moment at the Np site is of the localized character. The 5*f* electrons, as it were, possess the dual nature: the local moment at the Np site and the contribution of the 5*f* electrons to the volume of the Fermi surface. It is important to consider the quadrupolar interaction for the understanding of the high-field magnetization in $NpRhGa_5$ [91].

The discovery of non-magnetic heavy-fermion superconductors $PuCoGa_5$ (T_{sc}= 18.5 K) and $PuRhGa_5$ (T_{sc} = 9 K) has attracted attention because of its high T_{sc} and unconventional superconducting properties [93, 94]. The susceptibility of $PuRhGa_5$ increases with decreasing temperature, following the Curie-Weiss law with an effective magnetic moment of the $5f^5$ (Pu^{3+}) configuration, but indicates a sudden drop of the susceptibility due to onset of superconductivity [95], as shown in Fig. 53(b). From the result of the upper critical field, the topology of the Fermi surface is most likely cylindrical as in $CeCoIn_5$, as shown in Fig. 66(a) [95], although the dHvA experiment was not carried out because of the high H_{c2} value at lower temperatures. Theoretically, three kinds of cylindrical Fermi surfaces are proposed on the basis of the 5*f*-itinerant band model for $PuCoGa_5$ [96], as shown in Fig. 67(a).

Finally we note the recently discovered superconductivity of $NpPd_5Al_2$ with the tetragonal structure [97]. The crystal structure of $NpPd_5Al_2$ is similar to the tetragonal structure of $CeCoIn_5$ and $PuCoGa_5$, as shown in Fig. 68. The$5s^25p^1$ ($4s^24p^1$) electrons of the In(Ga) atoms in $CeCoIn_5$ ($PuCoGa_5$) are, however, replaced by the 4*d* electrons of the Pd atom in NpPdAl. The 4*d* electrons are well hybridized with the 5*f* electrons, and produce the strongly correlated conduction electrons. $NpPd_5Al_2$ does not order magnetically. The corresponding magnetic susceptibility increases steeply with decreasing temperature, but a sudden drop of the susceptibility occurs below T_{sc} = 4.9 K due to the onset of superconductivity, as

shown in Fig. 53(c). This is very similar to that in $CeCoIn_5$. The electronic state of NpP_5dAl_2 is found to be located in the vicinity of the antiferromagnetically ordered state from the results of the magnetic susceptibility mentioned above and the negative value of the paramagnetic Curie temperature. In fact, the γ value is large, $\gamma = 200$ mJ/K^{2}mol at $T_{sc} = 4.9$ K, and is enhanced to be 390 mJ/K^{2}mol at 0 K from the entropy balance, as shown by the *dotted* line in Fig. 54(b). Furthermore, the low-temperature electrical resistivity does not follow the Fermi liquid relation, but indicates a *T*-linear dependence, as shown in Fig. 48(d). The large paramagnetic effect is reflected in the strong suppression of the upper critical field, as shown in Fig. 66(c) and the step-like increase of the magnetization at H_{c2}, as shown in Fig. 69(a). In the case of a typical *d*-wave superconductor $CeCoIn_5$, it is clarified that a large paramagnetic effect produces a first-order phase transition at H_{c2} , namely the step-like increase of the magnetization, below temperatures lower than 0.3 T_{sc} ($T_{sc} = 2.3$ K), as shown in Fig. 69(b) [81]. The similar phenomenon is realized in $NpPd_5Al_2$. Surprisingly, the step-like increase of magnetization is observed up to a high temperature of 3 K (= 0.6 T_{sc}).

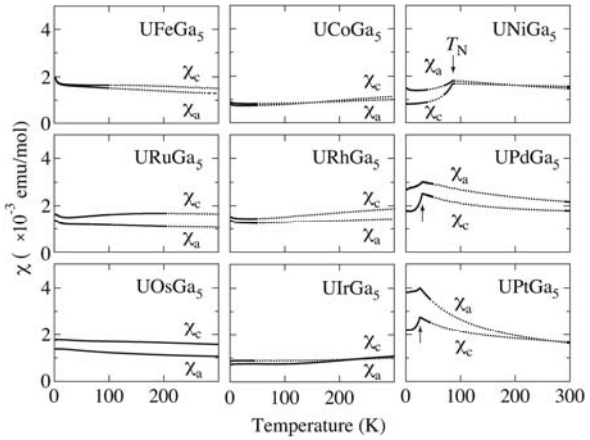

Fig. 55. Temperature dependence of the magnetic susceptibility in $UTGa_5$ (T: transition metal).

It is noticed that the normal and superconducting properties of $NpPd_5Al_2$ are very similar to those of $CeCoIn_5$, but the anisotropy of the magnetic susceptibility and the upper critical field is different from each other. If we simply analyze the anisotropy of the upper critical field from the so-called effective mass model, it is deduced that the Fermi surface is of a pan-cake shape. The corresponding Fermi surface based on the 5*f*-itinerant band model is, however, quasi-two dimensional, as shown in Fig. 67(c) [98]. It might be necessary to consider the anisotropic spin susceptibility between *H*|| [1 0 0] and [0 0 1], because the upper critical field is suppressed due to the large paramagnetic effect.

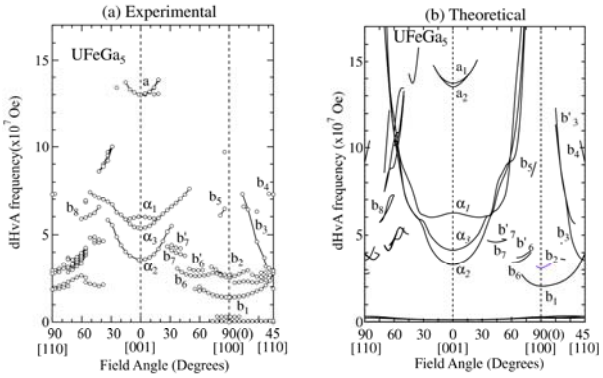

Fig. 56. Angular dependence of the dHvA frequency and the theoretical one in a Pauli paramagnet $UFeGa_5$.

6. Summary

The various kinds of electronic states in the cubic RX_3 and AnX_3 compounds, and the tetragonal RTX_5 and $AnTX_5$ compounds are studied from the point of view of Fermi surface properties and unconventional superconductivity, which are summarized as follows:

1) The Fermi surface properties in RX_3 and AnX_3 are mainly discussed from a divalent (Yb^{2+}) Pauli paramagnet $YbIn_3$ to a paramagnet $PuIn_3$, passing through a non-4*f* reference compounds $LaIn_3$, an antiferromagnet $NdIn_3$, an antiferromagnetic Kondo compound $CeIn_3$, $CeIn_3$ under pressure, another divalent (Yb^{2+}) Pauli paramagnet $YbPb_3$, another non-4*f* reference compound $LaSn_3$, an enhanced Pauli paramagnet UAl_3, a 4*f*-itinerant $CeSn_3$, 5*f*-itinerant USi_3, UGe_3 and USn_3, another enhanced Pauli paramagnet $NpGe_3$, including antiferromagnets UGa_3, UIn_3 and $NpIn_3$.

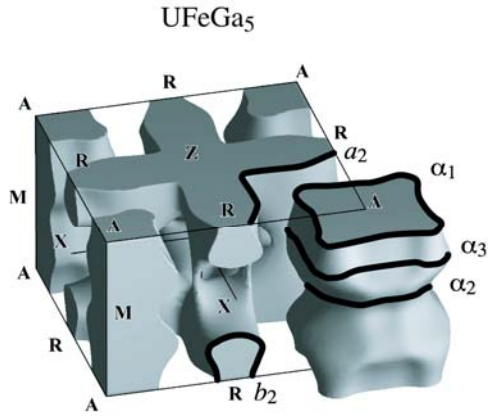

Fig. 57. Theoretical band 15 electron-Fermi surfaces based on a 4f-itinerant band model in a Pauli paramagnet $UFeGa_5$.

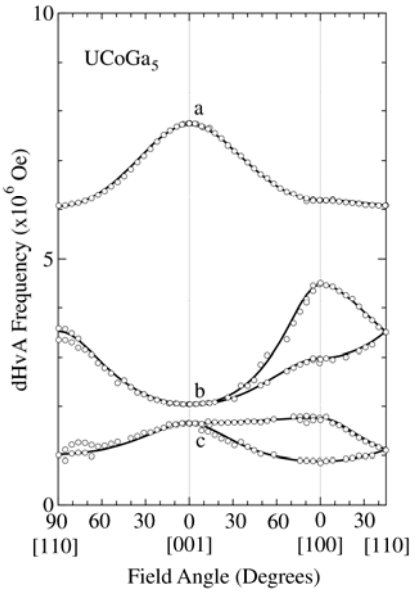

Fig. 58. Angular dependence of the dHvA frequency in a Pauli paramagnet $UCoGa_5$.

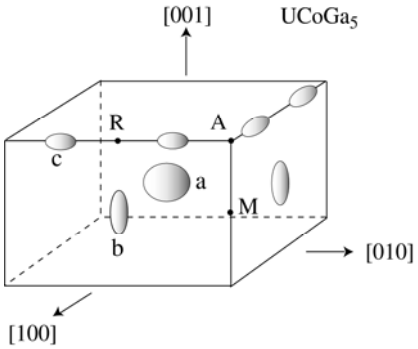

Fig. 59. Proposed Fermi surfaces in a Pauli paramagnet $UCoGa_5$.

It is clarified from the results of dHvA experiment and energy band calculation that the topology of the Fermi surfaces in enhanced paramagnets such as $CeSn_3$, UAl_3, UX_3 (Si, Ge, Sn), $NpGe_3$ and $PuIn_3$ is well explained by the *f*-itinerant band model. A marked change of the electronic states is observed in the dHvA experiment under pressure. The antiferromagnet Kondo compound $CeIn_3$ is found to be tuned to a non-magnetic heavy fermion compound at pressure P_c= 2.6 GPa. Unconventional *d*-wave type superconductivity appears in this pressure region. The first-order phase transition from the 4*f*-localized electronic state to the 4*f*-itinerant state occurs at P_c=2.6 GPa. The similar phase transition occurs in an antiferromagnet Kondo compound $CeRhIn_5$ at P_c = 2.35 GPa.

2) The Fermi surface properties are also studied in RTX_5 and $AnTX_5$. The Fermi surface properties of high-quality single crystals of RTX_5 and $AnTX_5$ are discussed from a non-4*f* reference compound $LaRhIn_5$ to the non-magnetic heavy-fermion superconductors $PuCoGa_5$ and $PuRhGa_5$, passing through an antiferromagnet $CeRhIn_5$, $CeRhIn_5$ under high pressure, a heavy-fermion superconductor $CeCoIn_5$, another reference compound $ThRhIn_5$, a paramagnet $UFeGa_5$, a semimetal $UCoGa_5$, and antiferromagnets $UPtGa_5$ and $NpRhGa_5$. These compounds are quasi-two dimensional, except $UCoGa_5$, possessing nearly cylindrical Fermi surfaces. It is interesting to note that the superconducting transition temperature $T_{sc} \approx 0.2$ K in $CeIn_3$ at 2.6 GPa with the three-dimensional electronic state is enhanced up to T_{sc} = 2.3 K in $CeCoIn_5$, and furthermore T_{sc} = 18.5 K in PuCoGa. The corresponding electronic specific heat coefficient is about 1000 mJ/Kmol in $CeIn_3$ around 2.6 GPa, 1070 mJ/K^2mol in $CeCoIn_5$ and 77 mJ/K^2mol in $PuCoGa_5$. A relatively large band width, together with quasi-two dimensionality, enhances the T_{sc} value, which can be extended to a large T_{sc} value of high-cuprates, where the itinerant 3*d*-electrons in the CuO_2 plane are responsible for superconductivity.

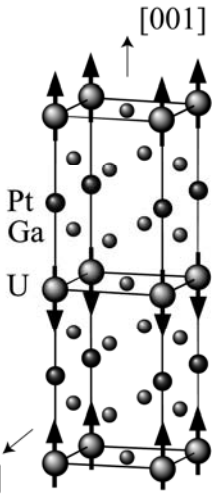

Fig. 60. Antiferromagnetic structure of $UPtGa_5$.

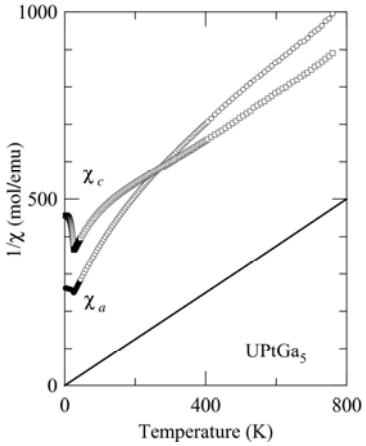

Fig. 61. Temperature dependence of the inverse magnetic susceptibility in $UPtGa_5$. A solid line corresponds to the free ion value of and 5 configurations.

3) It is emphasized that superconductivity of $CeCoIn_5$ and $NpPd_5Al_2$ is realized in an incomplete heavy fermion state. The usual heavy fermion state is formed below $T_{\chi max} \approx 20$ K and superconductivity occurs far below $T_{\chi max}$, namely at $T_{sc} = 0.5$ K in UPt_3, for example, whereas the magnetic susceptibility in $CeCoIn_5$ and $NpPd_5Al_2$ increases steeply at low temperatures but drops below $T_{sc} = 2.3$ K in $CeCoIn_5$ and $T_{sc} = 4.9$ K in $NpPd_5Al_2$ due to the onset of superconductivity. The corresponding electronic specific heat coefficient in $CeCoIn_5$ is 380 mJ/K^{2}mol, but is enhanced to be 1070 mJ/K^{2}mol at 0.25 K, which were clarified by measuring the specific heat in magnetic fields. Similar behavior of the specific heat is most likely realized in $NpPd_5Al_2$. This is the reason why the Fermi liquid nature is broken in both compounds under zero magnetic field. On applying pressure, both compounds approach the Fermi liquid nature, and loose considerably the heavy fermion state. Correspondingly, superconductivity disappears completely at pressures higher than 4.5 GPa in $CeCoIn_5$ [84, 99] and 5.5 GPa in $NpPd_5Al_2$[100]. Both compounds are thus located in the vicinity of the quantum critical point, and are accelerated to deviate from the quantum critical point with increasing pressure. The present incomplete heavy fermion state corresponds to a kind of the magnetic state, although the magnetic ordering is not realized. It is thus suggested that the strongly correlated conduction electrons might choose the magnetic state instead of phonons to form Cooper pairs with the *d*-wave type. Further experiments are necessary to clarify the superconductivity for these compounds, which are left to future studies.

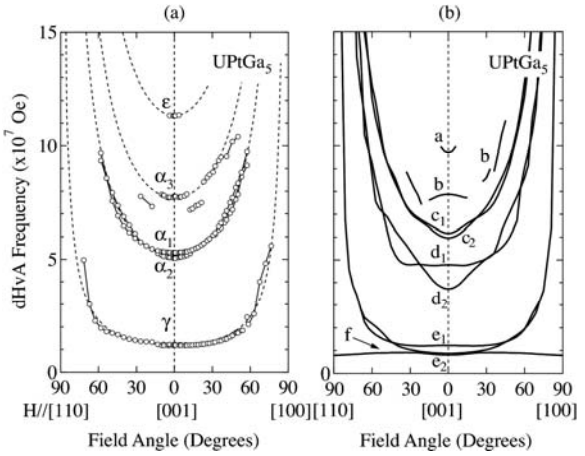

Fig. 62. Angular dependence of (a) the dHvA frequency and the theoretical one based on the spin (orbital)-polarized 5f-itinerant band model in an antiferromagnet $UPtGa_5$.

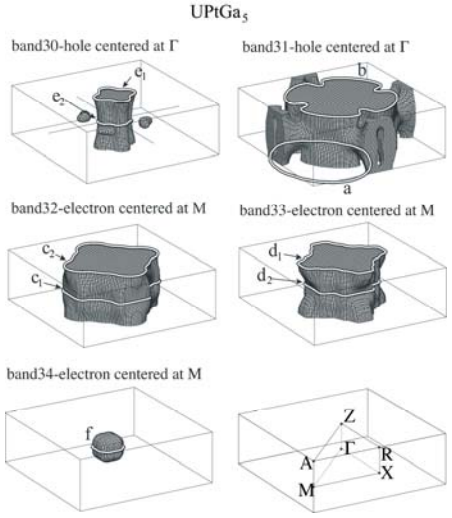

Fig. 63. Theoretical Fermi surfaces based in an antiferromagnet $UPtGa_5$.

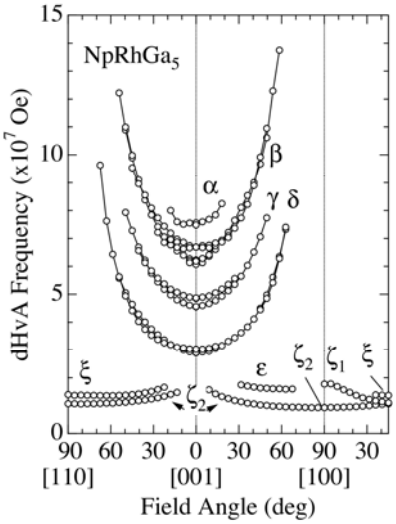

Fig. 64. Angular dependence of the dHvA frequency in an antiferromagnet $NpRhGa_5$.

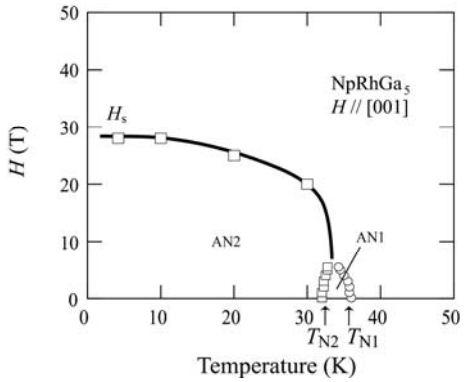

Fig. 65. Magnetic phase diagram for H|| [0 0 1] in $NpRhGa_5$.

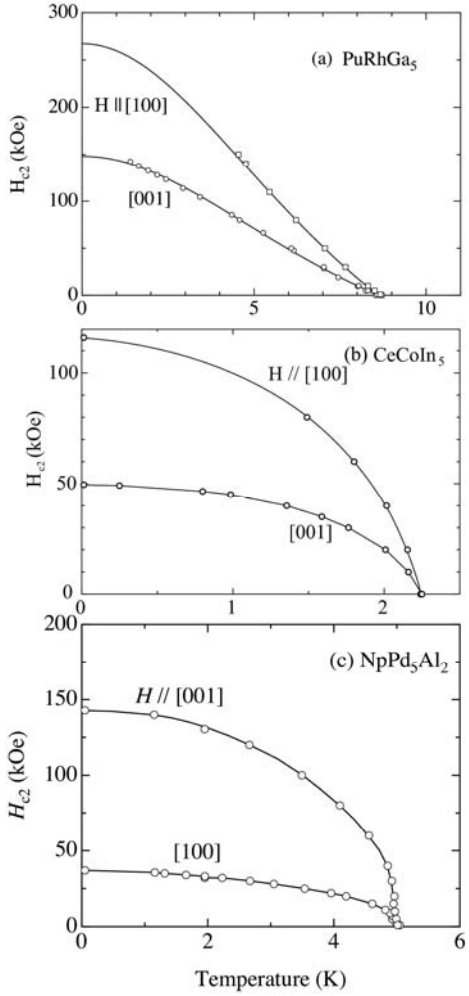

Fig. 66. Temperature dependence of the upper critical field in (a) $PuRhGa_5$, (b) $CeCoIn_5$ and (c) $NpPd_5Al_2$.

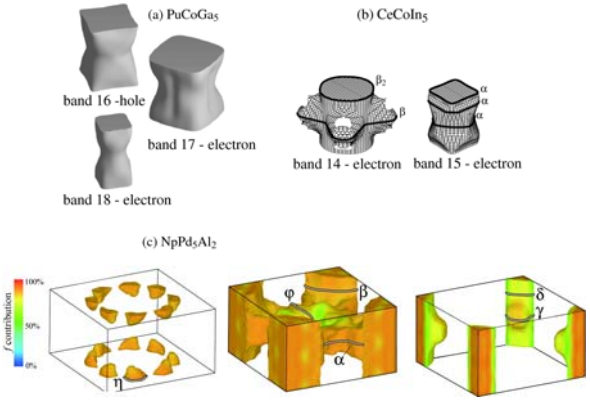

Fig. 67. Theoretical Fermi surfaces based on the f-itinerant band model in (a) $PuCoGa_5$ [96], (b) $CeCoIn_5$ [54] and (c) $NpPd_5Al_2$ [98].

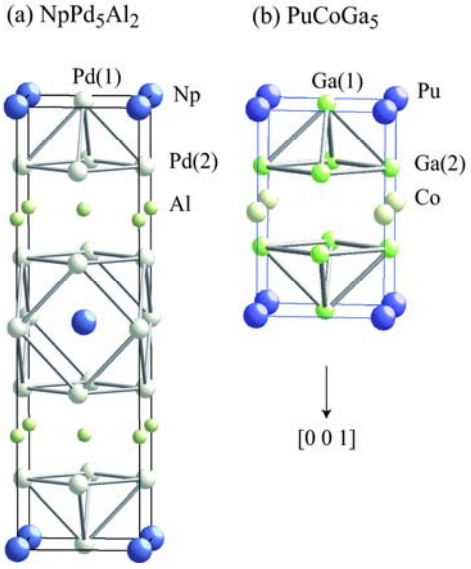

Fig. 68. Crystal structure of actinide superconductors (a) $NpPd_5Al_2$ and (b) $PuCoGa_5$.

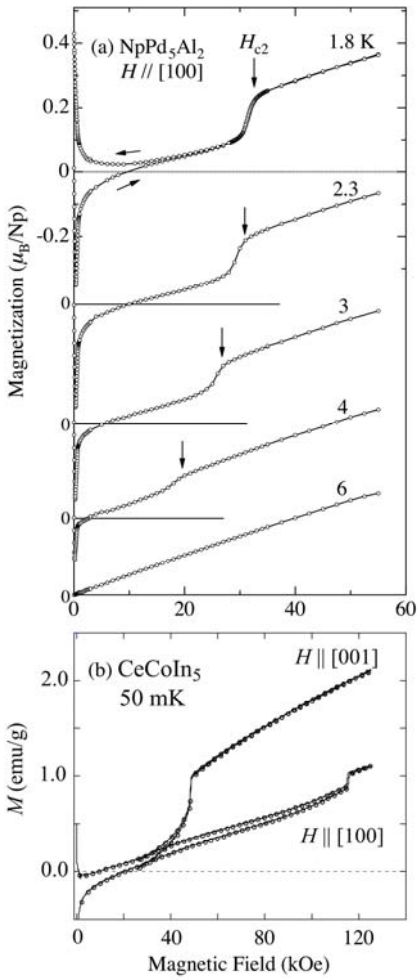

Fig. 69. Magnetization curves of (a) $NpPd_5Al_2$ [97] and (b) $CeCoIn_5$ [81], revealing a step-like increase of the magnetization at H_{c2} .

Acknowledgments

We are very grateful to K. Miyake, Y. Kitaoka and H. Yasuoka for helpful discussions. The present work was financially supported by Grants-in-Aid for Scientific Research (A), (C), Young Scientists (A). Scientific Research on Priority Areas and Creative Scientific Research (15GS0213) from the Japan Society for the Promotion of Science.

References

[1] Y. Ōnuki, T. Goto, T. Kasuya, Materials Science and Technology, ed. K. H. J. Buschow (VCH, Weinheim, 1991) Vol. 3A, Part I Ch. 7, p. 545.
[2] Y. Ōnuki, A. Hasegawa: Handbook on the Physics and Chemistry of Rare Earths, eds. K. A. Gschneidner Jr., and L. Eyring (Elsevier Science, Amsterdam, 1995) Vol. 20 p.1.
[3] Y. Ōnuki, R. Settai, K. Sugiyama, T. Takeuchi, T. C. Kobayashi, Y. Haga, E. Yamamoto, J. Phys. Soc. Jpn. **73**, 769 (2004).
[4] S. Doniach, Valence Instabilities and Related Narrow Band Phenomena, ed. R.D. Parks (Plenum, New York, 1977), p. 169.
[5] Y. Ōnuki, Y. Inada, H. Ohkuni, R. Settai, N. Kimura, H. Aoki, Y. Haga, E. Yamamoto, Physica B **280**, 276 (2000).
[6] M. Sigrist, K. Ueda, Rev. Mod. Phys. **63**, 239 (1991).
[7] N. Metoki, Y. Haga, Y. Koike, Y. Ōnuki, Phys. Rev. Lett. **80**, 5417 (1998).
[8] N. Bernhoeft, N. Sato, B. Roessli, N. Aso, A. Heiss, G. H. Lander, Y. Endoh, T. Komatsubara, Phys. Rev. Lett., **81** 4244 (1998).
[9] N. K. Sato, N. Aso, K. Miyake, R. Siina, P. Thalmeier, G. Varelogiannis, C. Geibel, F. Steglich, P. Fulde, T. Komatsubara, Nature, **410**, 340 (2001).
[10] M. Kyogaku, Y. Kitaoka, K. Asayama, C. Geibel, C. Schank, F. Steglich, J. Phys. Soc. Jpn. **62**, 4016 (1993).
[11] H. Tou, Y. Kitaoka, K. Ishida, K. Asayama, N. Kimura, Y. Ōnuki, E. Yamamoto, Y. Haga, K. Maezawa, Phys. Rev. Lett. **80**, 3129 (1998).
[12] K. Tenya, M. Ikeda, T. Sakakibara, E. Yamamoto, K. Maezawa, N. Kimura, R. Settai, Y. Ōnuki, Phys. Rev. Lett. **77**, 3193 (1996).
[13] D. Jaccard, H. Wilhelm, K. Alami-Yadri, E. Vargoz, Physica B, **259-261**, 1 (1999).
[14] N. D. Mathur, F. M. Grosche, S. R. Julian, I. R. Walker, D. M. Freye, R. K. W. Haselwimmer, G. G. Lonzarich, Nature **394**, 39 (1998).
[15] S. S. Saxena, P. Agarwal, K. Ahilan, F. M. Grosche, R. K. W. Haselwimmer, M. J. Steiner, E. Pugh, I. R. Walker, S. R. Julian, P. Monthoux, G. G. Lonzarich, A. Huxley, I. Sheikin, D. Braithwaite, J. Flouquet, Nature **406**, 587 (2000).
[16] D. Aoki, A. Huxley, E. Ressouche, D. Braithwaite, J. Flouquet, J. P. Brison, E. Lhotel, C. Paulsen, Nature **413**, 613 (2001).
[17] T. Akazawa, H. Hidaka, T. Fujiwara, T. C. Kobayashi, E. Yamamoto, Y. Haga, R. Settai, Y. Ōnuki, J. Phys.: Condens. Matter **16**, L29 (2004).
[18] H. R. Ott, Z. Fisk, in Handbook on the Physics and Chemistry of the Actinides, ed. A. J. Freeman and G. H. Lander (Elsevier Science, Amsterdam, 1987), Vol. **5**, Chap. 2, p.85.
[19] Y. Haga, H. Sakai and S. Kambe, J. Phys. Soc. Jpn., **76**, 051012 (2007).
[20] Y. Ōnuki, R. Settai, K. Sugiyama, Y. Inada, T. Takeuchi, Y. Haga, E. Yamamoto, H. Harima, H. Yamagami, J. Phys.: Condens. Matter **19**, 125203 (2007).
[21] Y. Okuda, Y. Miyauchi, Y. Ida, T. Yamada, Y. Ooduchi, T. D. Matsuda, Y. Haga, T. Takeuchi, K. Kindo, M. Hagiwara, H. Harima, K. Sugiyama, R. Settai, Y. Ōnuki, J. Phys. Soc. Jpn. **76**, 044708 (2007).
[22] Y. Haga, T. Honma, E. Yamamoto, H. Ohkuni, Y. Ōnuki, M. Ito, N. Kimura, Jpn. J. Appl. Phys. **37,** 3604 (1998).
[23] D. Shoenberg, Magnetic Oscillations in Metals (Cambridge University Press, Cambridge, 1984).
[24] R. Settai, T. Takeuchi, Y. Ōnuki, J. Phys. Soc. Jpn. **76,** 051003 (2007).
[25] Y. Ōnuki, R. Settai, K. Sugiyama, T. Takeuchi, T. C. Kobayashi, Y. Haga and E. Yamamoto, Physica B **300**, 61 (2001).
[26] Y. Haga, E. Yamamoto, Y. Tokiwa, D. Aoki, Y. Inada, R. Settai, T. Maehira, H. Yamagami, H. Harima, Y. Ōnuki, J. Nucl. Sci. Technol. Suppl. **3**, 56 (2002).
[27] D. D. Koelling, B. D. Dunlap, G. W. Crabtree, Phys. Rev. B, **31**, 4966 (1985).
[28] K. Sugiyama, T. Iizuka, D. Aoki, Y. Tokiwa, K. Miyake, N. Watanabe, K. Kindo, T. Inoue, E. Yamamoto, Y. Haga, Y. Ōnuki, J. Phys. Soc. Jpn. **71**, 326 (2002).
[29] H. H. Hill, Plutonium and Other Actinides, ed. W. N. Miner (AIME, New York, 1970), 2.
[30] H. Aoki, S. Uji, A. K. Albessard, Y. Ōnuki, Phys. Rev. Lett. **71,** 2110 (1993).
[31] R. Settai, H. Shishido, S. Ikeda, Y. Murakawa, M. Nakashima, D. Aoki, Y. Haga, H. Harima, Y. Ōnuki, J. Phys.: Condens. Matter, **13**, L627 (2001).
[32] N. Kimura, T. Tani, H. Aoki, T. Komatsubara, S. Uji, D. Aoki, Y. Inada, Y. Ōnuki, Y. Haga, E. Yamamoto, H. Harima, Physica B, **281 & 282**, 710 (2000).
[33] Y. Inada, H. Yamagami, Y. Haga, K. Sakurai, Y. Tokiwa, T. Honma, E. Yamamoto, Y. Ōnuki, T. Yanagisawa, J. Phys. Soc. Jpn., **68**, 3643 (1999).
[34] H. Sugawara, T. D. Matsuda, K. Abe, Y. Aoki, H. Sato, S. Nojiri, Y. Inada, R. Settai, Y. Ōnuki, Phys. Rev. B, **66** 134411 (2002).
[35] C. D. Bredl, F. Steglich and K. D. Schotte, Z. Phys. B, **29**, 327 (1978).
[36] C. D. Bredl, J. Magn. Magn. Mater., **63** & **64,** 355 (1987).
[37] T. Ebihara, I. Umehara, A. K. Albessard, K. Satoh Y. Ōnuki, J. Phys. Soc. Jpn., **62**, 1472 (1992).

[38] Y. Ōnuki, Y. Haga, E. Yamamoto, Y. Inada, R. Settai, H. Yamagami, H. Harima, J. Phys.: Condens. Matter, **15,** S1903 (2003).
[39] H. P. van der Meulen, Z. Tarnawski, A. de Visser, J. J. M. Franse, J. A. A. J. Perenboom, D. Althof, H. van Kempen, Phys. Rev. B, **41,** 9352 (1990).
[40] K. Sugiyama, M. Nakashima, D. Aoki, K. Kindo, N. Kimura, H. Aoki, T. Komatsubara, S. Uji, Y. Haga, E. Yamamoto, H. Harima, Y. Ōnuki, Phys. Rev. B, **60,** 9248 (1999).
[41] I. Harris, G. Raynor, J. Less-Common Met. **9**, 7 (1965).
[42] S. Nojiri, Y. Katayama, D. Aoki, N. Suzuki, K. Sugiyama, R. Settai, Y. Inada, Y. Ōnuki and H. Harima, Physica B, **281 – 282**, 747 (2000).
[43] I. Umehara, N. Nagai, Y. Ōnuki, J. Phys. Soc. Jpn., **60**, 591 (1991).
[44] A. Hasegawa, in Crystalline Electric Field Effects in f-Electron Magnetism, eds. R. P. Guetin, W. Suski and Z. Zolnierek (Plenum, New York), p.201
[45] I. Umehara, T. Ebihara, N. Nagai, K. Satoh, Y. Fujimaki, Y. Ōnuki, J. Phys. Soc. Jpn., **61**, 1633 (1992).
[46] R. Settai, T. Ebihara, H. Sugawara, N. Kimura, M. Takashita, H. Ikezawa, K. Ichihashi and Y. Ōnuki, Physica B, **201** 102 (1994).
[47] P. Lethuillier, J. Pierre, G. Fillion, B. Barbara, Phys. Stat. Sol., **A15**, 613 (1973).
[48] A. Czopnik, N. Iliev, B. Stalihski, C. Bazan, H. Madge, R. Pott, Physica B, **130**, 259 (1985).
[49] J. M. Lawrence, S. M. Shapiro, Phys. Rev. B, **22,** 4379 (1980).
[50] T. Ebihara, I. Umehara, A. K. Albessard, K. Satoh, Y. Ōnuki, Physica B, **186-188** (1993) 123.
[51] R. Settai, T. Kubo, T. Shiromoto, D. Honda, H. Shishido, K. Sugiyama, Y. Haga, T. D. Matsuda, K. Betsuyaku, H. Harima, T. C. Kobayashi, Y. Ōnuki, J. Phys. Soc. Jpn., **74**, 3016 (2005).
[52] T. D. Matsuda, Y. Haga, E. Yamamoto, S. Ikeda, H. Shishido, R. Settai, H. Harima, Y. Ōnuki, J. Phys. Soc. Jpn., **74** 3276 (2005).
[53] S. Araki, R. Settai, T. C. Kobayashi, H. Harima, Y. Ōnuki, Phys. Rev. B, **64**, 224417 (2001).
[54] H. Shishido, R. Settai, H. Harima, Y. Ōnuki, J. Phys. Soc. Jpn., **74**, 1103 (2005).
[55] I. Sakamoto, S. Ohara, I. Oguro, E. Yamamoto, Y. Haga, Y. Ōnuki, S. Maruno, J. Alloys and Compounds, **275-277** 505 (1998).
[56] D. Aoki, Y. Katayama, R. Settai, N. Suzuki, K. Sugiyama, K. Kindo, H. Harima, Y. Ōnuki, J. Phys. Soc. Jpn., **67** 4251 (1998).
[57] I. Umehara, N. Nagai, Y. Ōnuki, J. Phys. Soc. Jpn., **60**, 1294 (1991).
[58] A. Hasegawa, H. Yamagami, J. Phys. Soc. Jpn., **60**, 1654 (1991).
[59] I. Umehara, Y. Kurosawa, N. Nagai, M. Kikuchi, K. Satoh, Y. Ōnuki, J. Phys. Soc. Jpn. **59**, 2848 (1990).
[60] A. Hasegawa, H. Yamagami and H. Johbettoh, J. Phys. Soc. Jpn. **59**, 2457 (1990).
[61] A. Galatanu, Y. Haga, T. D. Matsuda, S. Ikeda, E. Yamamoto, D. Aoki, T. Takeuchi, Y. Ōnuki, J. Phys. Soc. Jpn., **74** 1582 (2005).
[62] D. Aoki, N. Watanabe, Y. Inada, R. Settai, K. Sugiyama, H. Harima, T. Inoue, K. Kindo, E. Yamamoto, Y. Haga and Y. Ōnuki, J. Phys. Soc. Jpn., **69**, 2609 (2000).
[63] P. Dervenagas, D. Kaczorowski, F. Bourdarot, P. Burlet, A. Czopnik and G. H. Lander, Physica B, **269**, 368 (1999).
[64] D. Aoki, N. Suzuki, K. Miyake, Y. Inada, R. Settai, K. Sugiyama, E. Yamamoto, Y. Haga, Y. Ōnuki, T. Inoue, K. Kindo, H. Sugawara, H. Sato and H. Yamagami, J. Phys. Soc. Jpn., **70** 538 (2001).
[65] Y. Tokiwa, D. Aoki, Y. Haga, E. Yamamoto, S. Ikeda, R. Settai, A. Nakamura, Y. Ōnuki, J. Phys. Soc. Jpn., **70** 3326 (2001).
[66] Y. Tokiwa, H. Harima, D. Aoki, S. Nojiri, M. Murakawa, K. Miyake, N. Watanabe, R. Settai, Y. Inada, H. Sugawara, H. Sato, Y. Haga, E. Yamamoto, Y. Ōnuki, J. Phys. Soc. Jpn., **69,** 1105 (2000).
[67] A. J. Arko, D. D. Koelling, Phys. Rev. B, **17**, 3104 (1978).
[68] D. Aoki, H. Yamagami, Y. Homma, Y. Shiokawa, E. Yamamoto, A. Nakamura, Y. Haga, R. Settai, Y. Ōnuki, J. Phys. Soc. Jpn., **74**, 2149 (2005).
[69] D. Aoki, Y. Homma, H. Sakai, S. Ikeda, Y. Shiokawa, E. Yamamoto, A. Nakamura, Y. Haga, R. Settai, Y. Ōnuki, J. Phys. Soc. Jpn., **75**, 084710 (2006).
[70] J. P. Sanchez, E. Colineau, P. Vulliet, K. Tomala, J. Alloys and Compounds, **275-277**, 195 (1998).
[71] Y. Haga, D. Aoki, H. Yamagami, T. D. Matsuda, K. Nakajima, Y. Arai, E. Yamamoto, A. Nakamura, Y. Homma, Y. Shiokawa, Y. Ōnuki, J. Phys. Soc. Jpn., **74**, 2889 (2005).
[72] A. Llobet, J. S. Gardner, E. G. Moshopoulou, J.-M. Mignot, M. Nicklas, W. Bao, N. O. Moreno, P. G. Pagliuso, I. N. Goncharenko, J. L. Sarrao and J. D. Thompson Phys. Rev. B, **69**, 024403 (2004).
[73] N. Metoki, J. Phys. Soc. Jpn., **75**, 24 (2006) Supplement,.
[74] F. Honda, N. Metoki, K. Kaneko, S. Jonen, E. Yamamoto, D. Aoki, Y. Homma, Y. Haga, Y. Shiokawa, Y. Ōnuki, Phys. Rev. B **74**, 144413 (2006).
[75] H. Shishido, R. Settai, D. Aoki, S. Ikeda, H. Nakawaki, T. Iizuka, Y. Inada, K. Sugiyama, T. Takeuchi, K. Kindo, T. C. Kobayashi, Y. Haga, H. Harima, Y. Aoki, T. Namiki, H. Sato, Y. Ōnuki, J. Phys. Soc. Jpn., **71**, 162 (2002).
[76] H. Hegger, C. Petrovic, E. G. Moshopoulou, M. F. Hundley, J. L. Sarrao, Z. Fisk and J. D. Thompson, Phys. Rev. Lett., **84** (2000) 4986.
[77] Y. Kitaoka, H. Mukuda, M. Yashima and A. Harada, J. Phys. Soc. Jpn., **76**, 051001 (2007).
[78] J. L. Sarrao, J. D. Thompson, J. Phys. Soc. Jpn., **76**, 051013 (2007).
[79] T. D. Matsuda, Y. Haga, E. Yamamoto, S. Ikeda, H. Shishido, R. Settai, H. Harima, Y. Ōnuki, J. Phys. Soc. Jpn., **76** 064712 (2007).

[80] K. Izawa, H. Yamaguchi, Y. Matsuda, H. Shishido, R. Settai, Y. Ōnuki, Phys. Rev. Lett. **87,** 057002 (2001).
[81] T. Tayama, A. Harita, T. Sakakibara, Y. Haga, H. Shishido, R. Settai, Y. Ōnuki, Phys. Rev. B, **65**, 180504(R) (2002).
[82] A. Bianchi, R. Movshovich, C. Capan, P. G. Pagliuso, J. L. Sarrao, Phys. Rev. Lett. **91**, 187004 (2003).
[83] K. Kakuyanagi, M. Saitoh, K. Kumagai, S. Takashima, M. Nohara, H. Takagi, Y. Matsuda, Phys. Rev. Lett. **94**, 0476202 (2005).
[84] H. Shishido, T. Ueda, S. Hashimoto, T. Kubo, R. Settai, H. Harima, Y. Ōnuki, J. Phys.: Condens. Matter, **15**, L499 (2003).
[85] Y. Tokiwa, T. Maehira, S. Ikeda, Y. Haga, E. Yamamoto, A. Nakamura, Y. Ōnuki, M. Higuchi and A. Hasegawa, J. Phys. Soc. Jpn., **70,** 2982 (2001).
[86] S. Ikeda, Y. Tokiwa, T. Okubo, Y. Haga, E. Yamamoto, Y. Inada, R. Settai, Y. Ōnuki, J. Nucl. Sci. Technol. Suppl., **3** 206 (2002).
[87] K. Kaneko, N. Metoki, N. Bernhoeft, G. H. Lander, Y. Ishii, S. Ikeda, Y. Tokiwa, Y. Haga and Y. Ōnuki, Phys. Rev. B, **68**, 214419 (2003).
[88] S. Ikeda, Y. Tokiwa, Y. Haga, E. Yamamoto, T. Okubo, M. Yamada, N. Nakamura, K. Sugiyama, K. Kindo, Y. Inada, H. Yamagami and Y. Ōnuki, J. Phys. Soc. Jpn., **72**, 576 (2003).
[89] D. Aoki, H. Yamagami, Y. Homma, Y. Shiokawa, E. Yamamoto, A. Nakamura, Y. Haga, R. Settai, Y. Ōnuki, J. Phys.:, Condens. Matter, **17,** L169 (2005).
[90] S. Jonen, N. Metoki, F. Honda, K. Kaneko, E. Yamamoto, Y. Haga, D. Aoki, Y. Homma, Y. Shiokawa, Y. Ōnuki, Phys. Rev. B, **74**, 144412 (2006).
[91] K. Sugiyama, H. Nakashima, D. Aoki, Y. Haga, E. Yamamoto, A. Nakamura, Y. Homma, Y. Shiokawa, K. Kindo, M. Hagiwara and Y. Ōnuki, J. Phys. Soc. Jpn. **75**, 094707 (2006).
[92] A. Kiss, Y. Kuramoto, J. Phys. Soc. Jpn. **75**, 034709 (2006).
[93] J. L. Sarrao, L. A. Morales, J. D. Thompson, B . L. Scott, G. R. Stewart, F. Wastin, J. Rebizant, P. Boulet, E. Colineau, G. H. Lander, Nature (London), **420**, 297 (2002).
[94] F. Wastin, P. Boulet, J. Rebizant, E. Colineau, G. H. Lander, J. Phys.: Condens. Matter **15**, S2279 (2003).
[95] Y. Haga, D. Aoki, T. D. Matsuda, K. Nakajima, Y. Arai, E. Yamamoto, A. Nakamura, Y. Homma, Y. Shiokawa, Y. Ōnuki, J. Phys. Soc. Jpn., **74**, 1698 (2005).
[96] T. Maehira, T. Hotta, K. Ueda, A. Hasegawa, Phys. Rev. Lett., **90**, 207007 (2003).
[97] D. Aoki, Y. Haga, T. D. Matsuda, N. Tateiwa, S. Ikeda, Y. Homma, H. Sakai, Y. Shiokawa, E. Yamamoto, A. Nakamura, R. Settai, Y. Ōnuki, J. Phys. Soc. Jpn., **76**, 063701 (2007).
[98] H. Yamagami, D. Aoki, Y. Haga, Y. Ōnuki J. Phys. Soc. Jpn., **76**, 083708 (2007).
[99] V. A. Sidorov, M. Nicklas, P. G. Pagliuso, J. L. Sarrao, Y. Bang, A. V. Balatsky, J. D. Thompson, Phys. Rev. Lett., **89**, 157004 (2002).
[100] F. Honda, C. S. Garde, T. Endo, R. Settai, D. Aoki, Y. Haga, T. D. Matsuda, N. Tateiwa, S. Ikeda, Y. Homma, H. Sakai, Y. Shiokawa, E. Yamamoto, A. Nakamura, Y. Ōnuki, to be published.

* Corresponding author. onuki@phys.sci.osaka-u.ac.jp